

Simulating brittle and ductile response of alumina ceramics under dynamic loading

Simons, E. C.; Weerheijm, J.; Sluys, L. J.

DOI

[10.1016/j.engfracmech.2019.05.013](https://doi.org/10.1016/j.engfracmech.2019.05.013)

Publication date

2019

Document Version

Accepted author manuscript

Published in

Engineering Fracture Mechanics

Citation (APA)

Simons, E. C., Weerheijm, J., & Sluys, L. J. (2019). Simulating brittle and ductile response of alumina ceramics under dynamic loading. *Engineering Fracture Mechanics*, 216, 1-20. Article 106481. <https://doi.org/10.1016/j.engfracmech.2019.05.013>

Important note

To cite this publication, please use the final published version (if applicable). Please check the document version above.

Copyright

Other than for strictly personal use, it is not permitted to download, forward or distribute the text or part of it, without the consent of the author(s) and/or copyright holder(s), unless the work is under an open content license such as Creative Commons.

Takedown policy

Please contact us and provide details if you believe this document breaches copyrights. We will remove access to the work immediately and investigate your claim.

1 Simulating brittle and ductile response of alumina ceramics 2 under dynamic loading

3 E.C. Simons^a, J. Weerheijm^{a,b}, L.J. Sluys^a

4 ^a*Delft University of Technology, P.O. Box 5048, 2600 GA Delft, The Netherlands*

5 ^b*TNO, P.O. Box 45, 2280 AA Rijswijk, The Netherlands*

6 Abstract

Alumina ceramic is often used in armour systems. This material is known to have a brittle response under tensile loading, while a ductile response is found when sufficiently high pressures are reached. During projectile impact a ceramic material experiences both tensile loading and high pressures, hence fails in both a brittle and ductile way. Properly capturing the ceramic failure in a single material model remains challenging. A viscosity regularized Johnson-Holmquist-2 model has been used to simulate dynamic loading on alumina ceramic. The simulations show that the brittle and ductile nature of the material can not be captured simultaneously in the current material model. A new failure strain formulation is proposed where the behaviour under tensile and compressive loading can be controlled independently. This allows to properly capture both the brittle and ductile response of the material in a single constitutive framework, with a single set of model parameters.

7 *Keywords:* ceramic, Johnson-Holmquist, ductile, brittle, failure

8 1. Introduction

9 Ceramic materials such as alumina and silicon carbide are widely used in armour systems. These ceramics have
10 a high hardness and relatively low weight when compared to traditional armour materials such as steel. The high
11 hardness of the ceramic ensures heavy deformation and even fracturing of incoming projectiles. The ceramic material
12 itself may also damage during this interaction. As long as the ceramic can exert a force on the projectile, the deforma-
13 tion and deceleration of the projectile continues. Understanding the failure process of a ceramic material is therefore
14 key in understanding the projectile/armour interaction [1, 2, 3]. Armour ceramics show multiple modes of failure.
15 Under tension the behaviour is brittle, while a more ductile behaviour can be found under compression. The brittle
16 nature under tensile loading is attributed to macro crack formation. While the ductile behaviour of the ceramics under
17 compression can be explained by micro-crack formation and plasticity. Plastic deformation of ceramics under impact
18 is well known and appears for sufficiently high confining pressures [4, 5, 6, 7, 8].

19 Although the main modes of failure are known for armour ceramics it is still difficult to properly capture their
20 behaviour, the sequence of occurrence and the interaction of mechanisms with a computational model. Experimental
21 measurements of the individual failure processes are very limited. True impact experiments with projectiles can
22 be performed, but material behaviour is often deduced rather than measured. The latter is difficult due to highly
23 varying stress states and the catastrophic nature of the experiments. There are two main paths one can take to better
24 understand the failure process. The first way is to limit the loading rates, and therefore consider quasi-static indentation
25 tests [9, 10] and slow dynamic testing such as drop-weight impact tests [7]. The main advantage of these tests is that
26 the ceramic does not fail catastrophically. This makes it possible to examine intermediate stages of failure which lie
27 between intact and fully failed. A second way to study ceramic failure is by simplifying the dynamic loading, e.g. by
28 plate impact or spall tests. In these experiments the material is loaded in a well defined way, which makes it possible
29 to deduce the material behaviour under these dynamic loading scenarios. When building a constitutive model for
30 ceramics this type of information is essential. The main advantage of the second type of tests over the first one is that
31 the dynamic nature of the impact problem is maintained, which is why the second approach is adopted in this paper.

32 Plate impact tests have been performed on ceramic materials over the past decades, providing a great deal of
33 information in literature [11, 12, 13, 14, 15, 16, 17, 18, 19, 20]. In a plate impact experiment high pressures can be

Nomenclature

A	intact deviatoric strength parameter	$\bar{\epsilon}_p^f$	equivalent plastic failure strain
B	residual deviatoric strength parameter	$\bar{\epsilon}_p^{f,min}$	minimum equivalent plastic failure strain
C	rate dependency parameter	$\bar{\epsilon}_p^{min}$	minimum equivalent plastic failure strain
d_1	deviatoric failure strain parameter	$\bar{\epsilon}_p^{max}$	maximum equivalent plastic failure strain
d_2	failure strain pressure dependency exponent	η	viscosity
D	scalar damage variable	$\dot{\lambda}$	rate of plastic multiplier
\dot{D}	rate of the scalar damage variable	$\dot{\lambda}_t$	threshold rate of plastic multiplier
E	Young's modulus	ν	Poisson's ratio
f	yield function	ρ	density
HEL	Hugoniot Elastic Limit	σ	stress tensor
m	residual strength pressure dependency exponent	σ_{eq}	Von Mises equivalent stress
n	intact strength pressure dependency exponent	σ_{HEL}	equivalent stress at HEL
p	pressure	σ_i	intact deviatoric material strength
p_c	maximum failure strain threshold pressure	σ_f	residual deviatoric material strength
p_t	minimum failure strain threshold pressure	σ_i^*	intact deviatoric material strength normalized to σ_{HEL}
P_{HEL}	pressure at HEL	σ_f^*	residual deviatoric material strength normalized to σ_{HEL}
T	hydrostatic tensile strength	σ_y	yield stress
T_0	rate independent hydrostatic tensile strength	σ_y^*	yield stress normalized to σ_{HEL}
T_t	hydrostatic tensile strength for transition rate		
ϵ	strain tensor	FE	Finite Element
$\dot{\epsilon}_0$	reference equivalent plastic strain rate	JH2	Johnson-Holmquist-2
$\dot{\epsilon}_p$	equivalent plastic strain rate	JH2-V	Viscosity regularized Johnson-Holmquist-2
$\dot{\epsilon}_p^*$	equivalent plastic strain rate normalized to $\dot{\epsilon}_0$		

34 reached and the material fails under compressive loading. The material is loaded in uniaxial strain and by measuring
35 the free surface velocity of the impacted plate the stress wave inside the material can be reconstructed. This stress
36 wave signal can then be used to derive material behaviour. Spall tests provide a second simplified loading scenario.
37 Two types of spall tests can be performed, either a slender bar [21, 22, 23, 24] of ceramic or a wide plate [25, 26, 27]
38 is loaded. Similar to plate impact a spall test performed on a plate will load the material in uniaxial strain conditions,
39 but in the spall test the target material fails under tension.

40 The plate impact and spall tests provide good insight in the material behaviour under pure compressive or tensile
41 loading. This information can be used to calibrate or validate a constitutive model. The constitutive model should
42 be able to capture the behaviour of the ceramic for both tests. This means that the model should be able to capture
43 the brittle and ductile behaviour under tension and compression. Multiple constitutive models for ceramics have been
44 proposed in literature over the past decades. Noteworthy models are those by Johnson and Holmquist [28, 29, 30],
45 Simha [31] and Deshpande-Evans [32, 33]. Most of the available ceramic material models are essentially softening
46 plasticity models. The main difference lies in the description of the material strength and the way the models deal
47 with ceramic failure. In the current paper the second model by Johnson-Holmquist [29] (JH2) is chosen as this is an
48 often used and widely accepted ceramic material model for ballistic impact.

49 Softening plasticity models (such as the JH2 model) are well known to suffer from mesh dependency. In [34] a
50 modification of the JH2 model was proposed which solved this mesh dependency. The modification consisted of the
51 inclusion of rate dependency (i.e. viscosity) on the hydrostatic tensile strength of the material. Adding a viscosity to a
52 constitutive model is known to provide an implicit length scale, which can regularize the solution and solve the mesh
53 dependency problem [35, 36, 37]. In addition to providing mesh independency for the JH2 model results it was seen
54 that the rate dependency of the tensile strength allowed the model to properly capture experimentally measured rate
55 dependency of the spall strength of ceramic [26], where the original JH2 model failed to do so.

56 The goal of the current paper is to find a generic model, capable of simulating ceramic failure both under tension
57 and compression, subjected to a range of loading rates. The viscosity regularized JH2 model (JH2-V) from [34] is
58 used as a starting point. This model will be described in Section 2. In Section 3 the JH2-V model (and the original
59 JH2 model) will be extensively tested. The models will be used to simulate a spall test, a plate impact tests, a
60 spherical impact test and a quasi-static ring-on-ring bending test. For a correct material model all of these tests should
61 give an adequate match between experiments and simulations, for a single set of model parameters. Unfortunately
62 the analysis shows that this is not true for the JH2-V model (or the JH2 model). Fortunately the simulation results
63 give a clear indication that this is related to the failure formulation of the model. The failure formulation in these
64 models only allows for either brittle failure under tension or ductile failure under compression. This is because the
65 damage rate in the failure formulation is a single pressure dependent function, coupling the behaviour under tension
66 and compression through the model parameters. In section 4 the failure formulation is modified such that the failure
67 response under tension and compression is separated. This allows independent control over the damage rate under
68 tensile and compressive loading. Calibration of the new formulation is done based on spall and plate impact tests. It
69 is shown that the JH2-V model with the new softening formulation can properly capture the ceramic's behaviour in
70 all four considered loading scenarios, for a single set of model parameters.

71 2. Methods and Models

72 Finite element (FE) simulations are performed. For the FE simulations a C++ based code is used, developed with
73 the open source FE libraries provided by JemJive[38]. Implicit solution schemes are used for the simulations in this
74 paper, Newton-Raphson for the quasi-static simulations and Hilbert-Hughes-Taylor- α for the dynamic simulations.

75 The choice for this numerical framework will be briefly explained by two comments. First a comment on the FE
76 method. This is a well established method to solve a partial differential equation (PDE). Other methods may also be
77 used, such as the material point method (MPM) [39, 40], smooth particle hydrodynamics (SPH) [41, 42, 43, 44, 45]
78 and many others. These methods may have some advantages and disadvantages over the FE method. One major
79 advantage of MPM and SPH is that these mesh-less methods easily deal with large deformations, but they tend to be
80 more computationally heavy than FEM. Since the test cases in the current paper do not experience large deformation
81 the FE method remains a good choice. The second comment is on the choice for the implicit time integration scheme.
82 Compared to explicit time integration schemes these implicit schemes have two main advantages. The first is that the
83 balance of linear momentum is exactly satisfied in each time step, which is not true for explicit schemes. The second

84 advantage is that these implicit schemes are unconditionally stable, and as such do not have a critical time step. This
 85 means time steps can be much larger than what is possible in explicit time integration schemes. This feature is further
 86 exploited in the current paper by using an adaptive time integration scheme, to keep the implicit scheme robust and
 87 fast. The Hilbert-Hughes-Taylor- α method furthermore has some damping included in its formulation, which may
 88 help when simulating dynamic contact problems [46]. The choice of how one solves the PDE and how one deals with
 89 time integration is independent of the material model. The constitutive model developed in the current paper should
 90 therefore be considered as a general model, not bound by the FEM or implicit time integration.

91 In the current paper the Johnson-Holmquist-2 [29] model is used, as this is a widely accepted material model for
 92 ceramics. The section will start with a short description of the material strength in this model, as well as the viscosity
 93 regularized formulation from [34]. The second part of the section will show how failure is captured in the ceramic
 94 material models JH2 and JH2-V, as well as several others.

95 2.1. Material strength

96 2.1.1. Johnson-Holmquist-2

97 In the Johnson-Holmquist-2 (JH2) model the yield function f of the material is described as

$$f(\boldsymbol{\sigma}, D) = \sigma_{eq}(\boldsymbol{\sigma}) - \sigma_y(\boldsymbol{\sigma}, D), \quad (1)$$

98 where $\boldsymbol{\sigma}$ is the stress tensor, D a scalar damage variable, σ_{eq} the Von Mises stress and σ_y the material strength. This
 99 material strength can be found as

$$\sigma_y^*(\boldsymbol{\sigma}, D) = (1 - D) \sigma_i^*(\boldsymbol{\sigma}) + D \sigma_f^*(\boldsymbol{\sigma}), \quad (2)$$

100 where * indicates that the values are normalized with respect to the equivalent stress at the Hugoniot elastic limit, i.e.
 101 σ_{HEL} . The material strength σ_y is an interpolation of the intact and residual strengths σ_i and σ_f with damage D . The
 102 intact and residual material strengths are a function of the pressure $p(\boldsymbol{\sigma}) = -\frac{1}{3}\sigma_{ii}$ and can be expressed as

$$\sigma_i^*(\boldsymbol{\sigma}) = A \left(\frac{T + p(\boldsymbol{\sigma})}{P_{HEL}} \right)^n (1 + C \ln \dot{\epsilon}_p^*), \quad (3)$$

$$\sigma_f^*(\boldsymbol{\sigma}) = B \left(\frac{p(\boldsymbol{\sigma})}{P_{HEL}} \right)^m (1 + C \ln \dot{\epsilon}_p^*). \quad (4)$$

103 Here A , B , C , n , m , T and P_{HEL} are material properties and $\dot{\epsilon}_p^*$ is the rate of equivalent plastic strain normalized with
 104 respect to reference rate $\dot{\epsilon}_0$. The rate dependency is controlled through parameter C . This rate dependency provides a
 105 deviatoric scaling of the material strength.

106 2.1.2. Johnson-Holmquist-2 Viscosity-regularized

107 In [34] a modification to the JH2 model was proposed. To solve mesh dependency of the original model an
 108 apex viscosity was introduced (hence Johnson-Holmquist-2 viscosity-regularized or JH2-V). The material strengths
 109 from (3) and (4) are now replaced by

$$\sigma_i^*(\boldsymbol{\sigma}) = A \left(\frac{T(\dot{\epsilon}_p) + p(\boldsymbol{\sigma})}{P_{HEL}} \right)^n, \quad (5)$$

$$\sigma_f^*(\boldsymbol{\sigma}) = B \left(\frac{p(\boldsymbol{\sigma})}{P_{HEL}} \right)^m. \quad (6)$$

110 In this formulation the apex pressure T is now a function of rate, providing a rate dependent tensile strength to the
 111 material. In the above formulations the original logarithmic rate dependency is absent, however the new formulation
 112 does not exclude the original formulation as both formulations may be used together.

113 The proposed apex viscosity is a mixed linear/logarithmic formulation

$$T(\dot{\epsilon}_p) = T(\dot{\lambda}) = \begin{cases} T_0 + \eta \dot{\lambda} & \text{for } \dot{\lambda} < \dot{\lambda}_t, \\ T_t \left(1 + \frac{\eta \dot{\lambda}}{T_t} \ln \left(\frac{\dot{\lambda}}{\dot{\lambda}_t} \right) \right) & \text{else.} \end{cases} \quad (7)$$

114 Here, $\dot{\lambda}$ is the rate of plastic multiplier, which is equal to the rate of equivalent plastic strain when using a deviatoric
 115 plastic flow rule. Furthermore, T_0 is the rate independent apex pressure, η is the viscosity and $\dot{\lambda}_t$ is the threshold rate
 116 for which the viscosity changes from linear to logarithmic. A transition pressure $T_t = T_0 + \eta\dot{\lambda}_t$ is also used in the
 117 formulation. The mixed linear/logarithmic formulation was found to provide mesh-independent results. In addition it
 118 was shown that the proposed viscosity formulation could match experimentally measured rate dependency of the spall
 119 strength of ceramics. The original strength formulation of the JH2 model failed to have mesh-independent results and
 120 also failed to capture the rate dependency in the spall strength.

121 2.2. Ceramic softening

122 A strength reduction in the JH2 and JH2-V models is achieved by the damage parameter D , as is shown in (2).
 123 This single damage parameter should be able to properly describe the underlying failure phenomena. This may be
 124 challenging since the failure behaviour of a ceramic under tension and compression can be very different. In this
 125 subsection damage growth of the JH2 model is compared to other models.

126 2.2.1. Johnson-Holmquist-2

127 In the JH2 model failure is a gradual process, where the yield stress reduces as the damage parameter D grows (as
 128 shown in (2)). The rate of damage is found as

$$\dot{D} = \frac{\dot{\bar{\epsilon}}_p}{\bar{\epsilon}_p^f}, \quad (8)$$

129 where $\dot{\bar{\epsilon}}_p$ is the rate of equivalent plastic strain and $\bar{\epsilon}_p^f$ is the plastic failure strain, for which the material is fully failed.
 130 The failure strain is not constant in the JH models but follows

$$\bar{\epsilon}_p^f(\sigma) = d_1 \left(\frac{T + p(\sigma)}{P_{HEL}} \right)^{d_2}, \quad (9)$$

131 where d_1 and d_2 are material constants. The values of d_1 and d_2 are typically unknown for a ceramic, because
 132 direct measurement of plastic failure strain in ballistic experiments is currently impossible. The functional form of
 133 the failure strain formulation in (9) is therefore an assumption and the parameters are determined through inverse
 134 modeling. Table 1 lists some of the failure related properties used in literature when modeling alumina ceramic. The
 135 material density is added to give insight in the type of alumina ceramic considered in these sources. The difference
 136 between highest and lowest values for d_1 and d_2 is found to be one order of magnitude. This great diversity is a clear
 137 indication of their level of uncertainty.

Table 1: JH2 failure strain constants for alumina ceramics

d_1	d_2	ρ [kg/m ³]	source
0.002	0.83	3625	[47]
0.005	0.83	3625	[48]
0.005	1.00	3700	[49]
0.010	1.00	3800	[50]
0.001	1.00	3890	[51]
0.010	0.07	3890	[52]
0.0125	0.70	3890	[53]

138 In the JH2 formulation the failure strain for $p < T$ is zero and failure is instantaneous. In the JH2-V model the
 139 rate dependent material strength allows for the material to reach $p < T$. However, if the JH2 failure strain is used this
 140 will still result in sudden failure. Tensile failure in ceramic material is related to fracture and thus crack propagation.
 141 Crack propagation is known to occur at a finite and limited velocity. This argues against the sudden failure found in
 142 the JH2 softening formulation. A simple modification can be made to (9) to ensure a finite rate of damage and at the
 143 same time allow pressure beyond the apex pressure. The failure strain formulation is changed to read

$$\bar{\epsilon}_p^f(\sigma) = \max \left(d_1 \left(\frac{T + p(\sigma)}{P_{HEL}} \right)^{d_2}, \bar{\epsilon}_p^{f,min} \right), \quad (10)$$

144 where $\bar{\epsilon}_p^{f,min}$ is a small but non-zero failure strain value. Please note that this is not the ‘modified formulation’ of
145 the failure strain as mentioned in the introduction. Equation (10) is merely a fix to allow the failure strain to exist
146 for pressures below the apex pressure. This is the formulation used to perform the initial comparative analyses in
147 Section 3. Later in Section 4 a completely new failure strain formulation will be proposed to improve the model
148 results.

149 2.2.2. Other ceramic models

150 The way the JH2 model deals with a reduction of strength is not unique. There are other softening plasticity
151 models for ceramics which use similar approaches. For instance the closely related Johnson-Holmquist-1 (JH1) and
152 the Johnson-Holmquist-Beissel (JHB) model, as presented in [28] and [30], respectively. These models use the same
153 damage parameter as the JH2 model. However, the gradual interpolation of the material strengths is not present in the
154 JH1/JHB models. Instead, for these models an intact strength is maintained until full failure is reached at $D = 1.0$, at
155 which there is a sudden transition to the residual strength. This approach essentially means that the ceramic behaves
156 perfectly plastic, with one sudden reduction of strength as full damage is reached.

157 Another approach is found in the Deshpande-Evans-2 (DE2) model [33]. In this model there are three distinct
158 failure mechanisms incorporated. Depending on the triaxiality $\zeta = \sigma_m/\sigma_e$, with mean stress σ_m and equivalent stress
159 σ_e , cracks grow: in pure tension, in tension/shear or do not grow. In this model the rate of damage increases as the
160 stress state is closer to hydrostatic tension. Also interesting to note is that a hardening response is found for high
161 compressive stress states.

162 A third approach is found in the material model by Simha [31]. In this model again three domains are identified,
163 based on the principal stress in the material. The rate of damage is then determined by the number of principal stresses
164 in tension, as well as the magnitude of the largest principal tensile stress. The difference between damage rate for
165 compression and hydrostatic tension is even in the order of 10^4 .

166 3. JH2-V model analysis

167 In the previous section multiple models for the failure behaviour of ceramics have been presented. In the current
168 section the JH2-V model with the original JH2 failure strain formulation from (10) is examined. The model is validated
169 with four different experimental tests: Spall, plate impact, spherical impact and quasi-static ring-on-ring bending. If
170 the JH2-V material model is valid, it should be able to match experimental results in all four tests, for a single set of
171 model parameters. This thorough analysis is meant to challenge and critically analyze the current material model. It
172 will reveal shortcomings of the material model. Based on the analysis in the current section an improved model will
173 be proposed in Section 4.

174 One comment should be made in advance regarding the experiments in this section. The experimental results are
175 obtained from literature. These experiments have all been performed on a similar high purity alumina ceramic. In
176 an ideal scenario they should have been performed on the exact same material, but unfortunately no such data set is
177 available. Small variations in the material properties are therefore expected and have to be accepted.

178 3.1. Spall simulations

179 Spall experiments on plate material are typically performed by impact. One plate of material is given an initial
180 velocity (the “impactor”) and impacts a plate of the same material (the “target”), as is shown in Figure 1. The
181 impacting plate generates a shockwave, which can lead to spall failure in the target material. The free surface velocity
182 of the target plate can be measured to determine the spall strength of the material. Given that the lateral dimensions
183 of the plates are much larger than the thickness, the central part of the plate experiences uniaxial strain. The problem
184 can thus be simplified to a single column of material, with an axial velocity applied to the bottom surface. This is also
185 shown in Figure 1, by the red dashed box.

186 Spall experiments on AL23 high purity alumina ceramics have been performed by Forquin’s group [26]. These
187 spall experiments were performed on alumina plates, but the stress wave was induced through an electromagnetic
188 device rather than impact. This allows for the generation of a more controlled stress wave, or as the authors state a
189 “shockless” spalling. In an earlier paper this experiment was simulated using the JH2 and JH2-V material models [34].
190 It was found that the original JH2 model with or without rate dependency fails to capture the rate effect under tension,

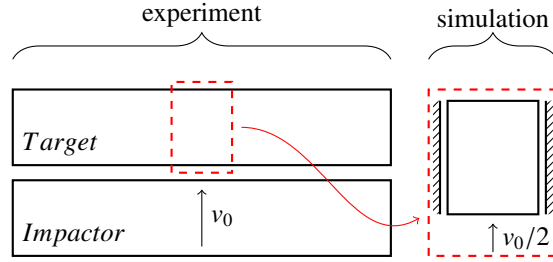


Figure 1: Plate impact experiment and simplified model. Due to the axial loading nature the problem can be simplified to a column of material, subjected to some applied velocity on its lower edge. In plate impact the impactor arrives with initial velocity v_0 and impacts on the target material, generating $v(t) = 0.5v_0$ if both materials are the same. Methods other than impact can also be used to apply a velocity profile, such as the “shockless spall” method from [26].

191 while the JH2-V model is able to capture the rate dependency measured in the spall strength of alumina ceramic.
 192 The current section briefly describes the simulations and results for the JH2-V model. The material properties from
 193 Table 2 in the column ‘Spall value’ are used in the simulations. These properties are based on [26], complemented
 194 by typical alumina values for the JH2 model from literature. Note that a minimal failure strain is imposed through
 195 equation (10) to allow a pressure below the (static) apex pressure T .

196 The spall test is simulated as a 10mm long and 2.5mm wide column, using linear three noded triangular elements
 197 under plane strain. The mesh is unstructured with element size $h \approx 0.1$ mm. A velocity is prescribed on the bottom
 198 of the column, while the top remains free to move. As mentioned before, the sides of the column are constrained
 199 from lateral movement. The applied velocities in the experiments are known. Idealized applied velocity profiles are
 200 presented in Figure 2a, which are the velocities applied in the simulations.

201 The predicted spall strength as a function of rate is shown in Figure 2b. The spall strength is defined as the highest
 202 axial stress found when apex failure is first experienced. The rate is the total axial strain rate experienced by the point
 203 of maximum stress at this moment. From the graph it is clear that a viscosity formulation with $\eta = 0.028 \cdot 10^{-3}$ GPa·s
 204 and $\dot{\lambda}_r = \infty$ is sufficient to capture the rate effect of the spall strength. For $\eta = 0.000$ GPa·s the rate independent
 205 JH2 formulation is retrieved. It can be seen that this model fails to capture the rate dependency. The rate independent
 206 model results are similar to the stress at which a yield surface is reached under tension, which is the ‘theoretical’
 207 strength in Figure 2b.

208 Figure 3 holds both the experimental and numerical predicted failure in the spall tests. Experimentally the ceramic
 209 could only be recovered from a single test. In this test the material was subjected to a wave similar to wave 2 from
 210 Figure 2a. The failure zones predicted in both simulations agree well with the experiment. The JH2-V model with
 211 zero viscosity shows a discrete failure pattern, typical for a material model suffering from mesh dependency. The
 212 viscous JH2-V model shows a more smooth damage profile, with intermediate values between intact and fully failed.
 213 Furthermore the viscous case shows damage extending beyond the experimentally observed failure zone. Whether
 214 this is also the case in the experiment is unknown, but the simulations performed in [26] also show non-zero crack
 215 densities beyond the cracked zone.

216 3.1.1. Spall - concluded

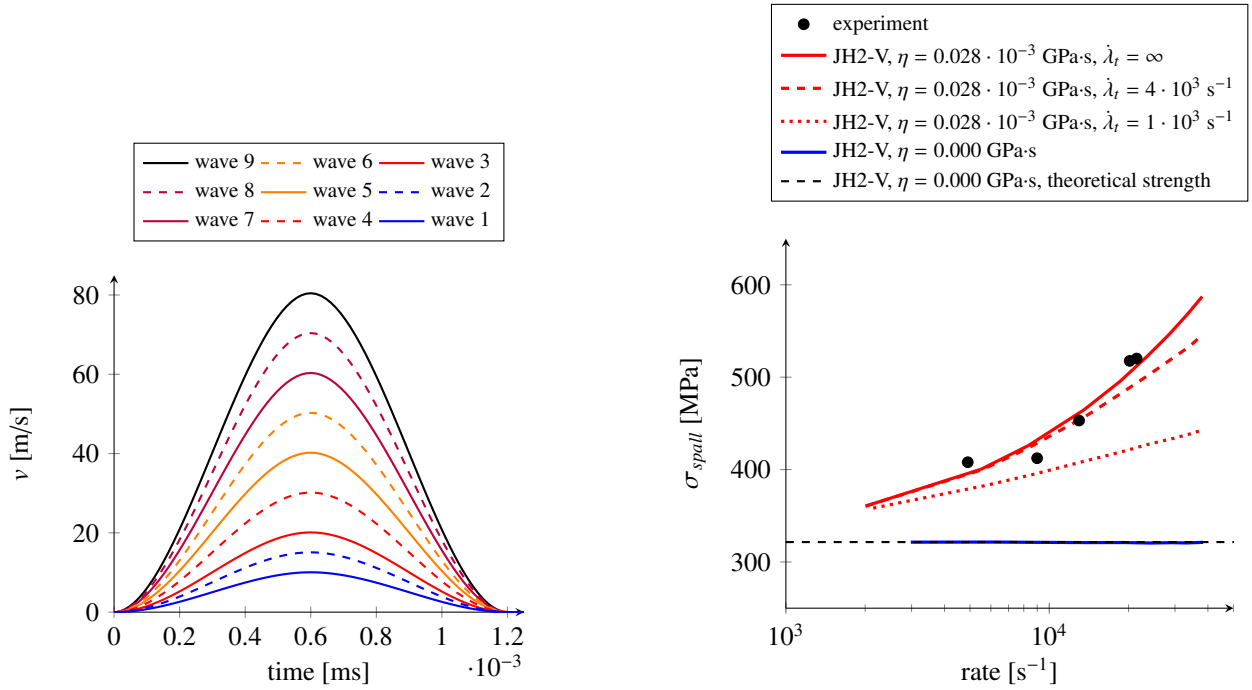
217 The spall simulations show that the rate dependent apex pressure in the JH2-V model allows to capture the rate
 218 effect under tension. The JH2 model fails to do so. This means that the apex viscosity is not only beneficial for
 219 regularization purposes, but it is also required in order to capture the (physical) rate dependent tensile strength.

220 3.2. Plate impact simulations

221 The spall simulations from the previous section show that the viscosity regularized JH2 model works well for
 222 alumina ceramics. The spall strength as a function of loading rate could be captured and (as far as experimental
 223 data are available) the failure zone was also found to be correct. In the current section the material is tested under
 224 compressive loading. Again a plate impact experiment is simulated, this time with a sufficiently high stress to cause
 225 failure under compression.

Table 2: JH2-V material properties used in simulations, based on [26] and complemented by typical alumina values for the JH2 model from literature. The initial model values are found in the column 'Spall value'. Modified parameter sets are found in the other columns, where bold face notation is used for the parameters different from the spall value.

variable	unit	Spall value	Plate impact value	variation 1 value	variation 2 value	variation 3 value	variation 4 value
E	GPa	360.0	380.0	380.0	380.0	380.0	360.0
ν	-	0.22	0.22	0.22	0.22	0.22	0.22
ρ	kg/m ³	3850	3890	3890	3890	3890	3850
A	GPa	0.930	0.930	0.930	0.930	0.930	0.930
B	GPa	0.310	0.310	0.810	0.310	0.310	0.310
n	-	0.6	0.6	0.6	0.6	0.6	0.6
m	-	0.6	0.6	0.6	0.6	0.6	0.6
C	-	0.0	0.0	0.0	0.0	0.0	0.0
T	GPa	0.2	0.2	0.2	0.2	0.2	0.2
η	GPa·s	$0.028 \cdot 10^{-3}$	$0.028 \cdot 10^{-3}$	$0.028 \cdot 10^{-3}$	$0.028 \cdot 10^{-3}$	$0.028 \cdot 10^{-3}$	$0.028 \cdot 10^{-3}$
λ_t	s ⁻¹	∞	∞	∞	$4 \cdot 10^4$	$4 \cdot 10^4$	∞
HEL	GPa	6.25	6.25	6.25	6.25	6.25	6.25
P_{HEL}	GPa	3.50	3.25	3.25	3.25	3.25	3.50
σ_{HEL}	GPa	4.125	4.50	4.50	4.50	4.50	4.125
d_1	-	0.005	0.005	0.005	0.050	0.500	0.500
d_2	-	0.75	0.75	0.75	0.75	0.75	0.75
$\epsilon_p^{f,min}$	-	$1.5 \cdot 10^{-4}$	$1.5 \cdot 10^{-4}$	$1.5 \cdot 10^{-4}$	$1.5 \cdot 10^{-4}$	$1.5 \cdot 10^{-4}$	$1.5 \cdot 10^{-4}$



(a) Applied velocity to induce a stress wave in the spall simulations.

(b) Spall strength, experimentally measured and predicted by simulation. Without viscosity the JH2-V model is not able to capture the rate dependency, but it gives a good match with experiments when $\eta = 0.028 \cdot 10^{-3}$ GPa·s and $\lambda_t = \infty$ are used.

Figure 2: Spall test on alumina ceramic, comparing experiments to simulations.

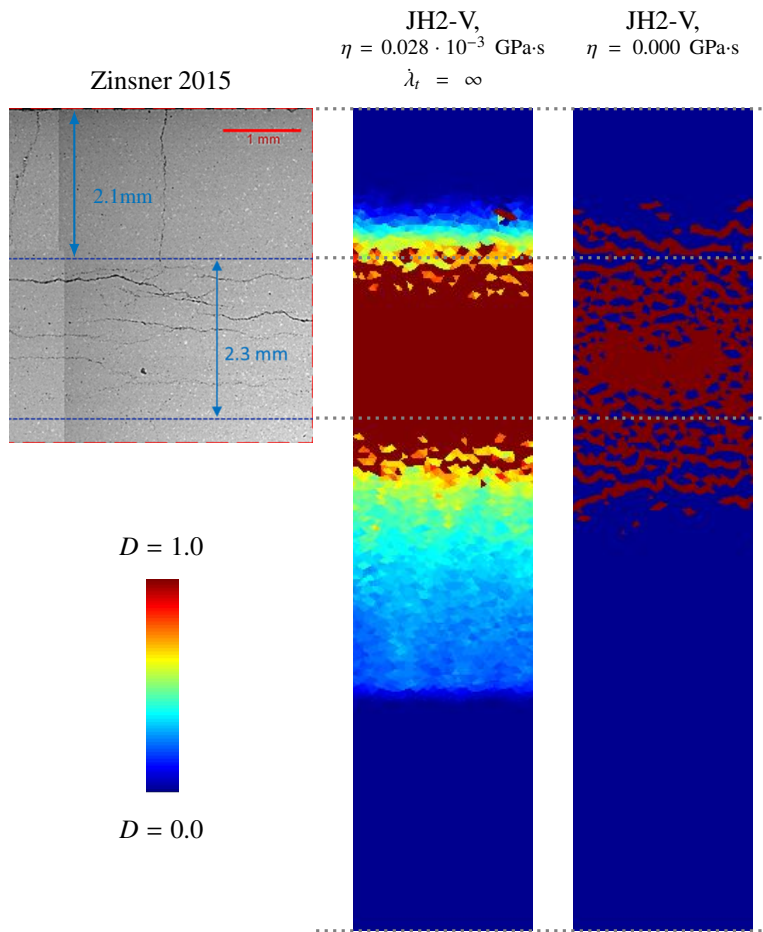


Figure 3: Damage profiles obtained in the spall experiment [26] and FE simulations. Stress wave 2 from Figure 2a is applied. The JH2-V material model with and without viscosity is compared.

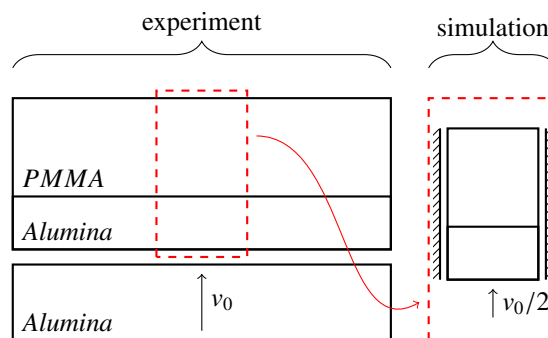


Figure 4: Plate impact experiment and simplified model. The alumina target material is backed by a PMMA plate. Due to the axial loading nature the problem can be simplified to a column of material, subjected to an applied velocity on its lower edge. In plate impact the impactor arrives with initial velocity v_0 and impacts on the target material, generating $v(t) = 0.5v_0$ if both materials are the same. Please note that the true thickness ratios are different from those depicted here.

226 In [54] results are reported for plate impact experiments on an aluminium oxide AD995, manufactured by the
227 Coors Porcelain corporation. In these experiments a 5mm thick alumina flyer plate was given an initial velocity v_0 .
228 This flyer plate impacted a 10mm thick alumina target, which was backed by 25.4mm thick PMMA material. The
229 impact velocity was such that the ceramic material failed under compression. The PMMA material was transparent,
230 which allowed for a velocity measurement of the interface alumina/PMMA. This velocity signal at the interface
231 contains information on the inelastic material behaviour. A schematic overview of the experiment is shown in Figure 4.

232 The plate impact experiment is simulated as a single column of four noded quadrilateral plane strain elements
233 elements, with the JH2-V material model. A constant element size $h = 0.01\text{mm}$ is used to mesh the column. A mixed
234 Gauss integration scheme is used, where $2*2$ integration is used for the deviatoric terms and 1 point integration for the
235 hydrostatic terms [55]. Similar to the spall simulations the lateral movements of this column are constrained, while
236 axial motion is allowed. The flyer plate is not modeled, instead a sudden velocity is applied on the target ceramic with
237 a magnitude of half the flyer plate velocity. This generates a sudden shock wave in the ceramic target material, which
238 will propagate as a stress wave. This idealized plate impact experiment is also shown on the right side in Figure 4.

239 The plate impact experiments in [54] report a material density of 3890kg/m^3 , which is slightly higher than what
240 was used in the spall experiments (i.e. 3850kg/m^3). Also the material stiffness is higher, 380GPa in the plate impact
241 and 360GPa for the spall test. It is important to correct these values as they affect the wave speed in the material,
242 which will in turn affect the interface velocity measurement obtained from the plate impact test. When changing the
243 elastic properties the shock related P_{HEL} and σ_{HEL} should also be modified, as these quantities are related to the HEL
244 of the material through the elastic constants. In the spall and plate impact experiments $HEL = 6.25\text{GPa}$, which gives
245 $P_{HEL} = 3.25\text{GPa}$ and $\sigma_{HEL} = 4.5\text{GPa}$ for the modified material stiffness. The full parameter set with modified values
246 can be found in the column 'Plate impact' from Table 2.

247 Figure 5 shows the experimental and numerical results for plate impact. The graph shows the velocity as a function
248 of time, measured at the ceramic/PMMA interface. The dotted lines show the experimental results while the solid lines
249 are used for the simulation results. An elastic stress wave arrives at the interface at point "A" in the graph. The velocity
250 is found to rapidly rise to point "B". At this point the material behaviour changes from elastic to inelastic. This point
251 is referred to as the Hugoniot elastic limit (HEL) of the material. After reaching the HEL the velocity continues
252 to rise until a maximum velocity is reached at "C". The behaviour between points "B" and "C" will be referred to
253 as the post-HEL behaviour. This post-HEL behaviour holds information on the ceramic strength during inelastic
254 deformation. After reaching point "C" the velocity remains constant until the material experiences unloading at "D".
255 This unloading is caused by wave reflection on the free surface of the flyer plate. In the simulations the focus lies on
256 the loading behaviour (post-HEL, from "B" to "C") and no unloading is applied. Simulations are therefore terminated
257 after $2\mu\text{s}$ and the unloading behaviour is not captured.

258 The experimental and numerical results can be compared in Figure 5. The arrival time of the stress wave and the
259 HEL are captured well, as are the peak plateau values for the first four impact velocities. However, the post-HEL
260 behaviour shows a major mismatch between experiments and simulations. This mismatch will be investigated closer
261 to find its origin.

262 3.2.1. Changing post-HEL behaviour

263 For plate impact tests the post-HEL behaviour is determined by the inelastic response of the ceramic material.
264 When using a material model such as the JH2-V model this relates to the plastic deformation and softening of the
265 material. The velocity profiles obtained from the simulations in Figure 5 indicate a rapid loss of material strength.
266 The experiments show a smooth post-HEL behaviour, indicating that failure of the material is more gradual and
267 strength is retained for a longer time. To introduce this effect in the JH2-V model the softening related parameter
268 d_1 and the viscosity parameters η and λ_t are obvious choices. However, in the JH2-V model the material strengths
269 (intact and residual) may also play a role. The intact strength can be directly obtained from experiments, thus is a
270 known quantity. The residual strength of ceramics is less certain, hence its effect on the post-HEL behaviour will be
271 considered, more specifically the effect of the B parameter from (6).

272 Figure 6 presents the velocity profiles for the spall test simulated with a larger residual strength. In the current
273 results $B = 0.81$, while the previous results were obtained with $B = 0.31$. The current results show a closer agreement
274 with the experiments. The post-HEL behaviour is now more smooth and also the peak plateau is reached at a time
275 comparable to experiments. Although the post-HEL velocities are lower than the experimental values it can be found
276 that increasing the B parameters improves the simulation results. It is however important to realize that there is almost

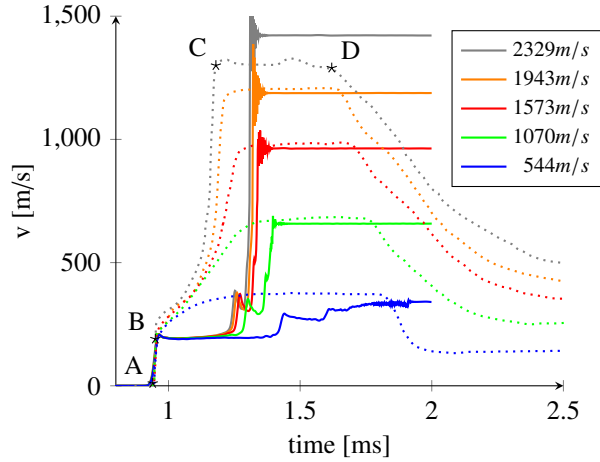


Figure 5: Simulation results for a plate impact test on alumina ceramic. The JH2-V model with the parameter set for the spall test is used, with a slightly increased material stiffness, density, P_{HEL} and σ_{HEL} . There is clearly a large difference in post-HEL behaviour. The dotted lines show the experimental results from [54], the solid lines are simulation results.

no loss in strength for the chosen value of residual strength, as $B = 0.81$ lies close to the intact strength parameter $A = 0.93$. It is known that a ceramic pulverizes under impact, which greatly reduces strength. So, although the plate impact results for simulations and experiments have a better match than before, it is not likely that this is a physically acceptable solution. There are other ways to retain a high material strength, such as a slower rate of damage.

The rate of damage in the JH2-V model is directly controlled by the failure strain formulation given in (9), as well as indirectly through the viscosity parameters η and λ_t . The most obvious way of lowering the rate of damage is by increasing the d_1 parameter. Figure 7 shows the plate impact results for $d_1 = 0.050$, which is a factor ten larger than the $d_1 = 0.005$ used in the spall simulations. This higher value of d_1 makes the behaviour more ductile. For these results it is clear that the post-HEL gives a more smooth behaviour. The lowest two impact velocities seem to match well with the experimental results. However, for the highest three velocities the post-HEL curve is convexly shaped. Both the experimental results and the simulation with a higher B show a more concave response.

The convexly shaped simulation response of the highest three impact velocities indicate that the damage rate is now too slow for these cases. To speed up the rate of damage one can change the viscosity parameters. Since the viscosity η was already determined by the spall test, only the threshold rate λ_t can be altered. It is important to choose a threshold rate which leaves the lowest two velocities unaffected since they already show good agreement between simulations and experiments. After some parametric study a threshold value $\lambda_t = 40 \cdot 10^3 \text{ s}^{-1}$ was selected. This value is higher than the maximum rate experienced in the 1070m/s test, but below the maximum experienced rate in the 1573m/s test. Figure 8 holds the results for the new threshold rate. This new threshold is found to improve the results as the higher impact velocity results now show a more concave response in the post-HEL behaviour. The current value of the threshold rate does not pose a problem for the spall simulations, as the threshold rate of $\lambda_t = 40 \cdot 10^3 \text{ s}^{-1}$ is not reached during the spall simulations. Changing the threshold rate improves the simulation results. There is however still delay in the highest impact results compared to experiments, which can be found in the post-HEL behaviour as well as the peak plateau arrival time. Additional parametric study showed that the results can improve further by increasing the d_1 parameter once more to $d_1 = 0.500$. Results for this parameter set can be found in Figure 9. The parameter sets introduced in this section are also shown in Table 2 in the columns labeled 'variation 1, 2, 3'. Since none of these three parameter sets appears to be better than the other, a deeper investigation is required.

3.2.2. Plate impact concluded

When moving from spall simulations to plate impact simulations it was clear that the JH2-V model with a single set of material parameters was not able to properly predict both experiments. A major mismatch was found in the post-HEL behaviour of the material. The largest contributions were found to come from material softening, viscosity and the residual strength. Altering material properties resulted in a good match between experiments and simulations.

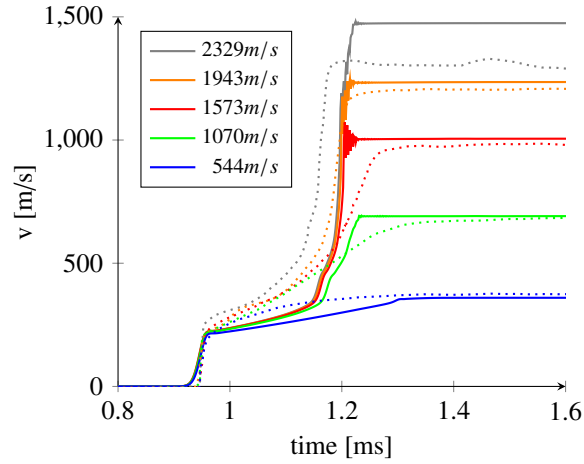


Figure 6: Simulation results for a plate impact test on alumina ceramic. The parameter set used to obtain Figure 5 was also used here, but the residual strength parameter B is now increased to $B = 0.81$. The post-HEL behaviour is now more smooth and the peak plateau arrival time is now also closer to the experimental values. The dotted lines show the experimental results from [54], the solid lines are simulation results.

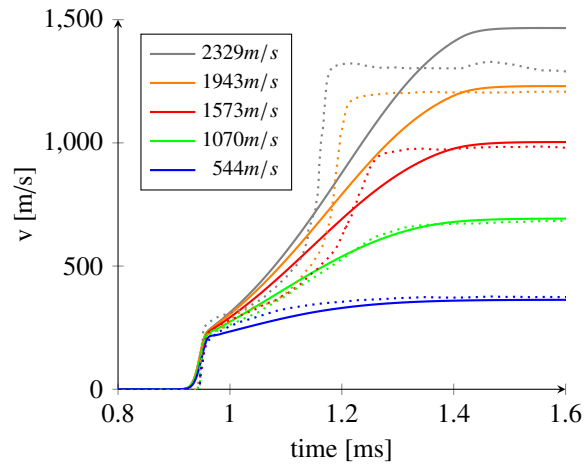


Figure 7: Simulation results for a plate impact test on alumina ceramic. The parameter set used to obtain Figure 5 was also used here, but with a softening parameter $d_1 = 0.050$. The dotted lines show the experimental results from [54], the solid lines are simulation results.

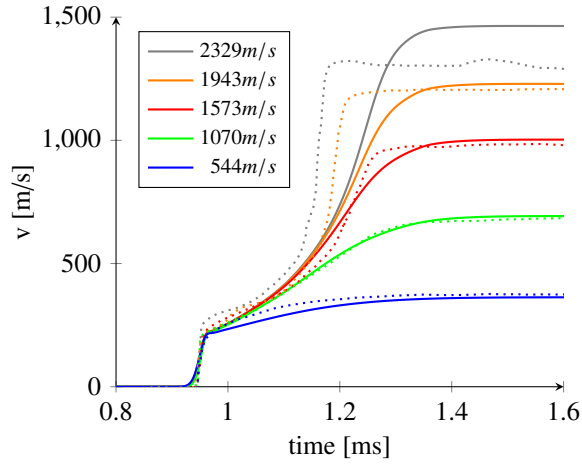


Figure 8: Simulation results for a plate impact test on alumina ceramic. The parameter set used to obtain Figure 5 was also used here, but with $d_1 = 0.050$ and $\lambda_t = 40000s^{-1}$. The dotted lines show the experimental results from [54], the solid lines are simulation results.

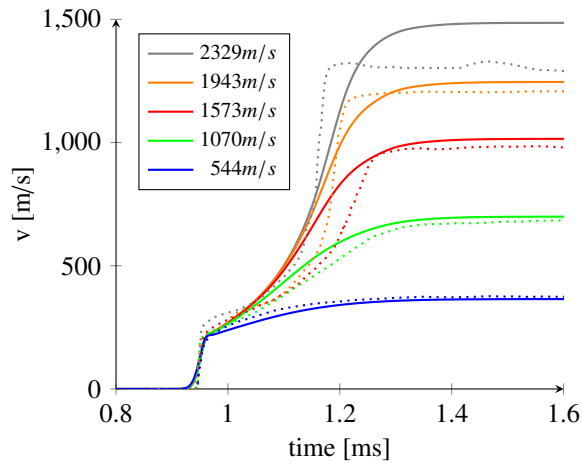


Figure 9: Simulation results for a plate impact test on alumina ceramic. The parameter set used to obtain Figure 5 was also used here, but with $d_1 = 0.500$ and $\lambda_t = 40000s^{-1}$. The dotted lines show the experimental results from [54], the solid lines are simulation results.

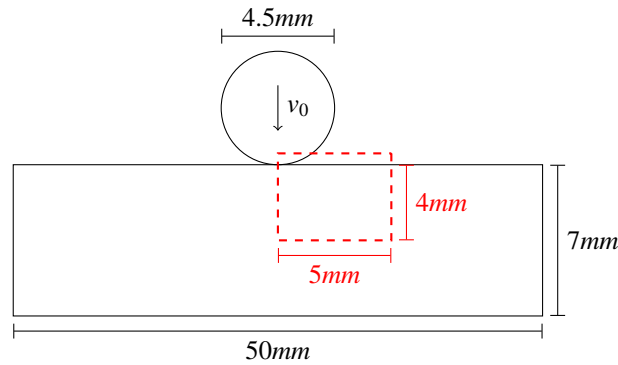


Figure 10: Spherical impact test, the projectile is given an initial velocity v_0 . Geometry of the simulated problem is given. The red dashed box is the spatial domain in which the simulation results will be presented. Note that the figure does not show the true aspect ratios.

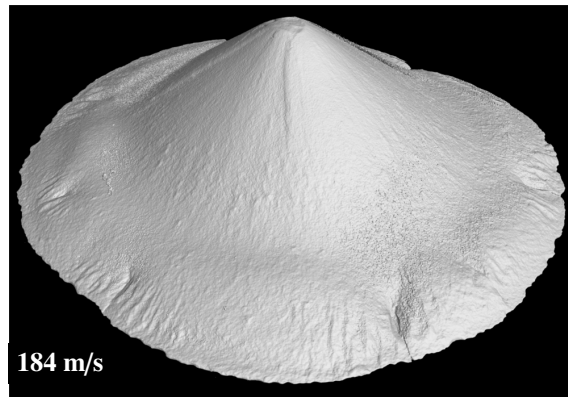
308 However the residual strength had to be increased by a factor three and the failure strain even by a factor ten or
 309 hundred. These changes can no longer be explained by small differences in the tested materials. Hence, these large
 310 variation in the model parameters indicate that there is an inconsistency in the formulation. The current results do
 311 however not show if the mismatch is caused by the softening/viscosity or the residual material strength. In the next
 312 subsections additional tests will be performed to further investigate the origin of this mismatch.

313 3.3. Spherical impact

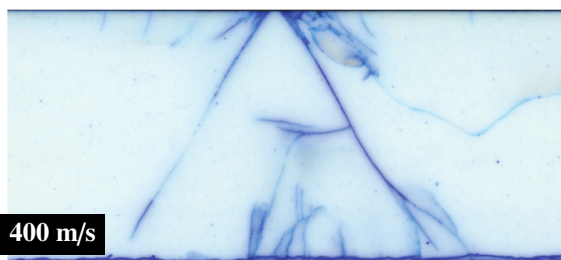
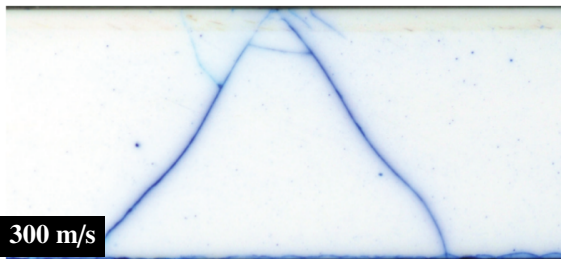
314 Two types of impact tests have been simulated and analyzed so far. One in which failure occurred under tension
 315 (spall test) and one where failure occurred under compressive loading (plate impact). In both cases a dense alumina
 316 ceramic was used and an uniaxial deformation was imposed. These two extremes in loading condition did not give
 317 a unique answer in terms of material properties. In the current section a spherical impact test is simulated where the
 318 deformation is far from uniaxial and a wide range of stress states is encountered. Compression, tension and mixed
 319 mode loading will be found in this test, which can help revealing the correct material model behaviour.

320 In spherical impact experiments a projectile is given an initial velocity v_0 and impacts on a target material. This
 321 test is schematically shown in Figure 10. In the current section a steel projectile is assumed to impact on a ceramic
 322 target material. During this interaction both the projectile and target undergo (in)elastic deformation. Experimental
 323 results of spherical impact on alumina ceramic and silicon carbide ceramic are shown in Figures 11a, 11b and 11c.
 324 The figures show that the main mode of failure in the ceramic is cone cracking. The silicon carbide results also show
 325 a dark zone directly below the impact site. This is referred to as the quasi-plastic zone, which is characterized by
 326 micro-cracking and even plastic deformation. It is important to notice that the material in this subsurface zone is not
 327 pulverized. Although there is damage to the material the strength has not yet reduced to its minimum. This knowledge
 328 will prove vital in analyzing the spherical impact results.

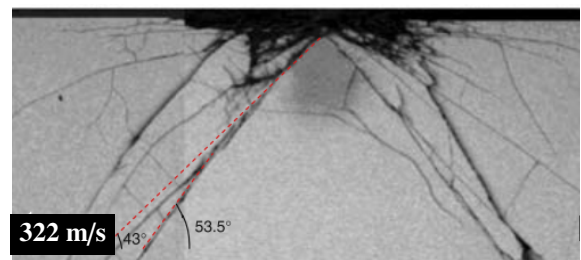
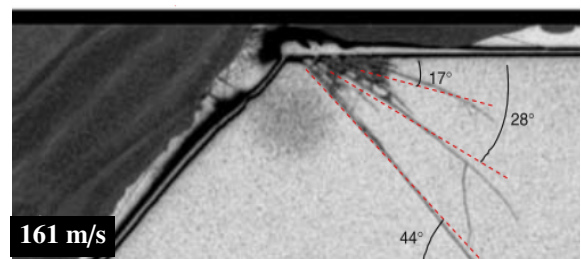
329 The spherical impact experiment is simulated. The projectile is assumed to be a sphere with a diameter of 4.5mm,
 330 made of SAE51200 ball bearing steel. A Johnson-Cook material model was used to simulate this steel material, with
 331 a yield stress of 2.2GPa and hardening parameters from [58]. In the current simulations temperature and rate effects
 332 on the yield stress of the steel are ignored. The target is a ceramic plate with a thickness of 7mm and lateral dimension
 333 of 50mm (see Figure 10). The ceramic plate is not supported and without any material attached to the back surface.
 334 The ceramic material itself is a high density alumina ceramic, similar to the material previously considered in the
 335 spall and plate impact experiments. For the ceramic material the JH2-V model is used. As base model parameters the
 336 values from the plate impact test are chosen, as well as the three variations introduced in the previous section. These
 337 parameter sets can be found in Table 2 in the columns 'Plate impact' and 'variation 1,2,3'. The variations correspond
 338 to the parameter sets used to obtain the plate impact results from Figures 6, 8 and 9. The sphere impact experiment
 339 is simulated in a 2d axi-symmetric formulation, with the axis of impact as obvious axis of symmetry. Any lateral
 340 movement is constrained along this axis of symmetry and no other boundary conditions are applied to the system. As
 341 such the ceramic can be considered a free standing or unsupported target. Three noded linear elements are used to



(a) An alumina ceramic cone, retrieved after a spherical impact experiment (E.P. Carton, TNO, personal communication, 2018). Figure was obtained by X-ray imaging (A. Thijssen, Delft University of Technology, personal communication, 2018).



(b) Alumina ceramic after spherical impact, pictures are obtained from [56]. Comminution of ceramic directly below the projectile is absent.



(c) Silicon carbide ceramic after spherical impact, pictures are obtained from [57]. A quasi-plastic zone is found below the projectile, but the material is not comminuted.

Figure 11: Experimental results for a steel sphere impacting ceramic tiles. Top figure shows the result of impact on a ceramic plate without backing, the bottom figures are cross-sections of ceramic plates with backing after impact. Projectile velocities are shown. Cone cracking is clearly visible in all cases.

342 mesh this problem. The mesh is unstructured and the element size ranges from $h \approx 0.05\text{mm}$ along the axis of impact
343 to $h \approx 1.0\text{mm}$ at the far side of the ceramic target. A penalty stiffness model with Coulomb friction ($\mu = 0.5$) is used
344 to describe the contact between projectile and target.

345 Figure 12 shows the ceramic damage after spherical impact using four different parameter sets for the JH2-V
346 model. The figures show only the material directly underneath the projectile corresponding to the dashed box shown
347 in Figure 10. For all cases the alumina ceramic is impacted by a steel sphere with an initial velocity of 200m/s. The
348 figures are taken after $1.4\mu\text{s}$ of simulated time. For the given tile thickness and elastic properties this is sufficient time
349 for the initial pressure wave to travel to the back surface of the ceramic tile and return to the impact surface. This time
350 is long enough to study the initiation of failure, but not enough to observe if the projectile is stopped by the ceramic.
351 Although the latter is interesting from a practical point of view, the former is sufficient to investigate the previously
352 found mismatch in parameters.

353 All cases show cone cracking (see Figure 12). However, the reference set and variation 1 of the model parameters
354 both show a zone of fully failed material ($D = 1.0$) directly underneath the projectile. From (2) it can be found
355 that these zones retain a strength under compression, but can no longer sustain any tensile loading. This is typical
356 behaviour of fragmented material, which is what a ceramic is expected to be after full failure under compressive
357 loading. Recall that full fragmentation was not observed in experiments (Figure 11), where some damage could be
358 found underneath the projectile but the ceramic was not pulverized. This shows that the parameter set with a fast
359 softening and the set with a high residual strength can not be correct. The variations 2 and 3, which have a slower
360 softening than the reference set, provide a better match with experiments. Variation 2, with $d_1 = 0.050$, shows a cone
361 crack as well as a (semi-) spherical zone of damage below the projectile. Although this is an improvement from the
362 fully failed top layer found for a fast softening these results would still indicate a fully comminuted material. The best
363 match with experiments is found for variation 3 with $d_1 = 0.500$, for which a clear cone crack forms. For this case
364 minor damage is predicted below the projectile ($D \approx 0.01$), but the material is not fully failed as in the other cases.
365 This minor damage is found from the figure as an ever so slightly light blue discolouration.

366 3.3.1. Spherical impact concluded

367 The plate impact and spall test have shown that it was impossible for the JH2-V model with a single parameter set
368 to match both sets of experimental results. It was argued that both softening/viscosity or residual strength could be
369 the reason for this mismatch. However, the spall and plate impact tests did not offer any certainty as to which option
370 was the correct one.

371 Spherical impact was proposed as a third test case. This experiment is often performed on armour ceramics,
372 where the main failure mechanism is cone cracking as well as some (incomplete) subsurface damage. Spherical
373 impact simulations showed that these mechanisms could only be predicted for material with a slow softening and
374 not for material with a high residual strength. So the spherical impact test has shown that the mismatch in earlier
375 simulations and experiments was caused by the softening and viscosity.

376 For the plate impact experiment it was shown that slow softening is required. In the spall test a fast softening was
377 assumed. However, it also would have been possible to use slow softening for the spall test and tune the viscosity
378 accordingly. So, although the previous experiments have shown that there is some mismatch between experiments
379 and simulations, the mismatch can still be solved by recalibration of the parameters. In the next section one more
380 experiment is considered to investigate this behaviour.

381 3.4. Ring on ring

382 Three types of tests have been performed so far, namely a spall test with pure tensile loading, a plate impact test
383 with pure compressive loading and a spherical impact test where a wide range of stress states including both tensile
384 and compressive stresses. The results for these tests have shown an inconsistency in the material softening modeling.
385 For the spall test a softening parameter $d_1 = 0.005$ was used, for which the material softening is fast and the response
386 may be considered as being brittle. However, plate and spherical impact showed good agreement with simulations
387 using $d_1 = 0.500$, for which the softening is slow and the response is more ductile. A possible solution to this
388 inconsistency would be to increase the softening parameter for the spall test. In fact, the spall experiments could also
389 be matched for $d_1 = 0.500$ by tuning the viscosity parameters. However, increasing d_1 would jeopardize the brittle
390 response of ceramics under tension. This would be highly unwanted since the brittle nature of (armour) ceramic under
391 tensile loading is a well accepted material trait.

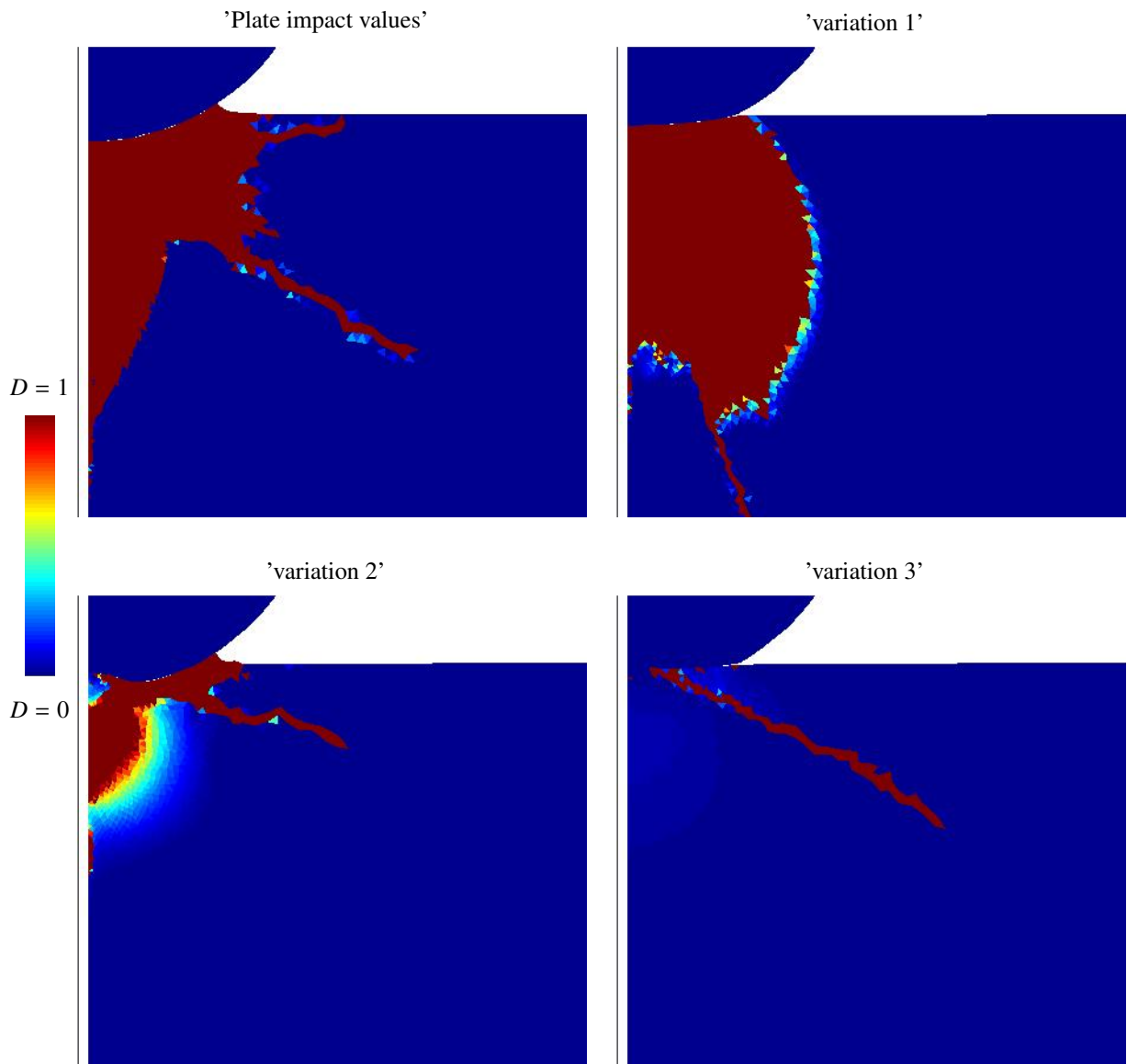


Figure 12: Spherical impact results for the JH2-V model. Damage variable $D \in [0..1]$ is shown after $1.4\mu\text{s}$ of simulated time.

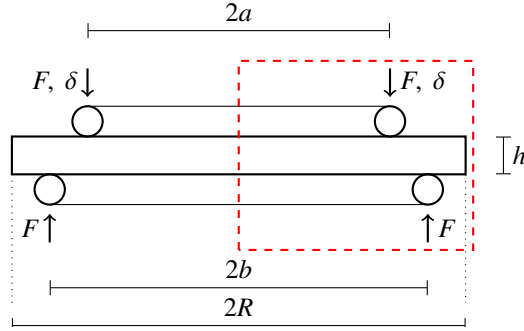


Figure 13: Ring on ring bending experiment. The red dashed box is the spatial domain which is used for a 2D axisymmetric simulation of the experiment.

392 A ring-on-ring (ROR) bending test is considered as final test. This is a tensile dominated test, where a disk of
 393 material is supported by a large ring on the bottom and loaded through a smaller ring on top. This creates a constant
 394 and bi-axial bending moment in the specimen inside the smaller ring. Figure 13 gives a schematic representation
 395 of the ring-on-ring test. The test is controlled by applying a deformation δ on the smaller inner ring, a force can
 396 then be measured either in the same ring or on the large bottom ring. The test is performed at a very slow loading
 397 rate ($\dot{\delta} = 0.1\text{mm/s}$), such that the test can be considered quasi-static and inertia effects can be excluded. The low
 398 loading rate removes the dynamic effects such as wave propagation and allows to focus solely on the material failure.
 399 Please note that the material rate dependency from the JH2-V model is still present, even though inertial effects are
 400 excluded by using quasi-static simulations. The only requirement is that there is some measure of (pseudo) time in
 401 the simulation, which can be found from the applied deformation rate $\dot{\delta} = 0.1\text{mm/s}$. This ensures the material model
 402 retains its regularizing properties.

403 An analytical solution for the stress field inside the specimen under ROR loading exists [59, 60]. This makes it
 404 possible to relate an applied force to a (tensile) stress in the disk and find the strength of the tested material. The
 405 tensile stresses in radial (σ_r) and tangential direction (σ_θ) at the bottom of the specimen, inside the internal ring can
 406 be given as

$$\sigma_r = \sigma_\theta = \frac{3F}{4\pi h^2} \left[2(1 + \nu) \ln\left(\frac{a}{b}\right) + \frac{(1 - \nu)(a^2 - b^2)}{R^2} \right], \quad (11)$$

407 where F is the applied force, ν the Poisson's ratio, h the specimen thickness and a, b, R the radii of the internal ring,
 408 external ring and specimen.

409 Experimental results for ROR bending on alumina ceramics are available in literature. In [61] an ultimate tensile
 410 stress of Wesgo alumina is presented ranging from 190 to 260MPa. In [26] the experimental results show the ultimate
 411 tensile stress ranges from 168.6–232.7MPa. Between these two sources the experimental set-up differs in dimensions
 412 and the alumina ceramics are similar but not exactly the same.

413 The geometry of the test as presented in [26] was assumed, such that $R = 9\text{mm}$, $a = 5\text{mm}$, $b = 8\text{mm}$ and $e = 1\text{mm}$.
 414 Since the ROR experiment was performed on the same material as the spall test the model parameters for spall are
 415 used as (brittle) base values. A more ductile behaviour is found by using $d_1 = 0.500$. The parameter sets used in the
 416 ROR simulations are those found in columns 'Spall' and 'variation 4' from Table 2. The ROR problem is simulated
 417 in a 2d axi-symmetric strain formulation. Here the center of the disk is considered as axis of symmetry, where all
 418 horizontal movement is constrained. Vertical movement is constrained for a single node on the bottom of the disk,
 419 at distance b . Vertical displacements are imposed on a single node on the top surface of the disk, at distance a .
 420 The mesh for this problem is unstructured and three noded linear triangular elements are used with a size $h \approx 0.025\text{mm}$.
 421 Figure 14 holds the force and displacement measured on the inner top ring during the simulation. The figure also
 422 shows two hatched zones corresponding to the experimental results from [61] and [26], for which the reported failure
 423 stresses were converted to forces using (11). When comparing to the experimental results it is clear that slow softening
 424 results in an overestimated material strength, while an acceptable material strength is found with fast softening of
 425 the material. The maximum stress found in the simulations was 240MPa and 329MPa for the fast and slow softening
 426 cases respectively.

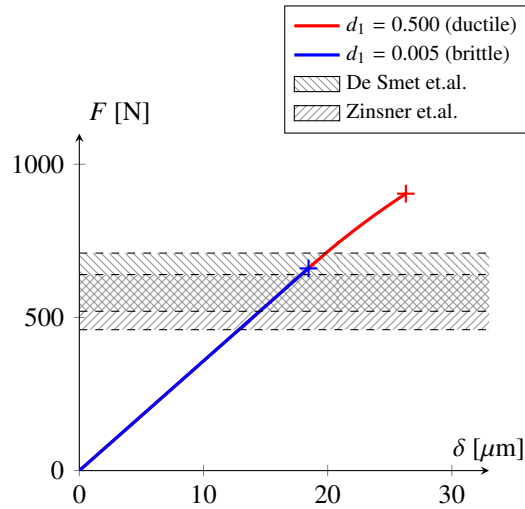


Figure 14: Ring on ring bending test. Results are obtained by simulation with the JH2-V material model, for two values of softening. The simulations fail to converge at the crosses, this is when a large number of points fail under apex return. This may be seen as the sudden and brittle failure of the specimen. The ultimate force for the two tests is found as 662N and 904N, corresponding to tensile stresses of 240MPa and 329MPa. Experimentally measured ranges from De Smet [61] and Zinsner [26] are given by the hatched areas.

3.4.1. Ring-on-Ring concluded

The ring-on-ring test confirms that a fast softening is required under tension. Earlier it was demonstrated that slow softening was required for the compression dominated tests. This shows the obvious need for a separation in material softening, where controlling the response under tension and compression independently is possible. The next section will show that a separated material softening can indeed be used to match all previously described experiments, with a single set of parameters.

4. JH2-V model improvement

The experiments and simulations in the previous sections have shown that the original failure strain formulation of the JH models is inadequate. The analyzed experiments could only be matched by changing softening related parameters and could not be captured by a single set of model parameters.

For a ceramic the failure mechanisms under compression and under tension are significantly different. Failure under tension occurs by brittle fracture of the material, while a ductile response can be found under sufficiently high compression. Under high compression failure is characterized by crystal plasticity and micro-cracking. If the failure mechanisms under tension and compression are so different, it is reasonable to also distinguish between these two mechanisms in the material model. The material models by Deshpande-Evans and Simha presented in the section 2 acknowledge that a ceramic material has multiple failure mechanisms. These models capture each of the different failure mechanisms by its own softening/damage behaviour. In the JH2 material model failure is captured by the failure strain formulation (9). This single formulation includes a pressure dependency, but does not offer a clear separation in behaviour for each of the failure mechanisms. In fact the function couples the behaviour under tension and compression through the softening parameters d_1 and d_2 . Because of this coupling, changing the failure strain under compression will inadvertently change the damage rate under tension and vice versa. In a recent publication the limited flexibility of the JH failure strain formulation (9) was also addressed [62], albeit for glass material using different strength formulations. In the publication a shift was proposed to the failure strain, to have zero plastic deformation to failure under low pressures and allow for accumulation of plasticity beyond some pressure threshold. This does indeed provide a clear separation between brittle tensile failure and more ductile compression failure. Such approach can however not be used in the current visco-plastic framework, since a non-zero plastic strain is required to activate viscosity and obtain regularization.

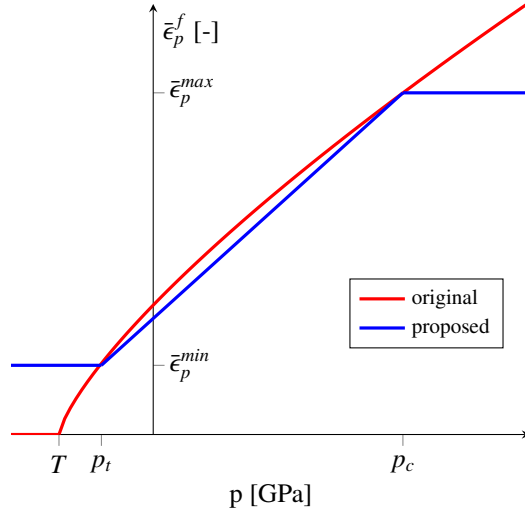


Figure 15: Failure strain as function of pressure, in the original JH2 and the proposed formulation.

454 A new softening formulation is proposed, in which the damage rate under tension and compression can be controlled independently. The formulation for the rate of damage can remain the same as (8). The failure strain formulation from (9) is replaced by the tri-linear equivalent plastic strain formulation

$$\bar{\epsilon}_p^f(\sigma) = \begin{cases} \bar{\epsilon}_p^{min}, & p(\sigma) < p_t \\ (\bar{\epsilon}_p^{max} - \bar{\epsilon}_p^{min}) \left(\frac{p(\sigma) - p_t}{p_c - p_t} \right) + \bar{\epsilon}_p^{min}, & p_t < p(\sigma) < p_c \\ \bar{\epsilon}_p^{max}, & p_c < p(\sigma). \end{cases} \quad (12)$$

457 This formulation assumes a failure strain $\bar{\epsilon}_p^{min}$ for pressures below p_t , a failure strain $\bar{\epsilon}_p^{max}$ for pressures above p_c and interpolates between these two values for intermediate pressures. This formulation allows for independent changes to the failure strain and thus damage rate under tension and compression. Furthermore, the model is simple, providing a clear advantage when calibrating the model as will be shown later in this section.

461 The proposed failure strain formulation is shown together with the original failure strain formulation in Figure 15. In this figure the failure strain is plotted for arbitrary model parameters. The proposed model parameters can be chosen such that the original formulation is linearly approximated in the domain $p_t < p < p_c$, but obviously this is not required.

465 The new formulation (12) requires information on the failure strains, as well as a pressure range for which the behaviour transitions from brittle to ductile. For brittle materials it is not uncommon to have a transition from brittle to ductile behaviour. Often this is linked to an ambient temperature, but a transition can also be found at a given confining pressure [63, 64, 65]. To use the proposed formulation one should ideally know the transition pressure. If this data is not available one may calibrate the model for a given test under tension and one under compression. The latter approach will be used in this paper.

471 The spall and plate impact tests from the previous section can be used to calibrate the newly proposed failure strain formulation. These tests provide insight in the failure behaviour under uniaxial tensile and compressive loading. Results from sections 3.1 and 3.2 showed that the failure strain might differ by a few orders of magnitude between uniaxial tensile or compressive loading. A first approximation of the model parameters in equation (12) can be obtained as follows.

476 First consider uniaxial tensile loading on a ceramic with the material properties from Table 2. Under these conditions the yield strength will be reached at a pressure $p_{min} = -0.17$ GPa. In the original failure strain formulation with $d_1 = 0.005$ this pressure leads to $\bar{\epsilon}_p^f(p_{min}) = 0.00015$. Similarly for uniaxial compressive loading a pressure of $p_{max} = 3.02$ GPa is found and $d_1 = 0.500$ leads to a failure strain of $\bar{\epsilon}_p^f(p_{max}) = 0.4965$. Here the original model parameter d_1 was chosen as the values for which spall and plate impact simulations agreed well with experimental

Table 3: JH2-V model parameters using the improved failure strain formulation from (12). The model parameter sets for each test are shown. Only the stiffness, density and Hugoniot pressure are changed, which is justified because of small differences in experimentally tested ceramics.

variable	unit	Spall value	Plate impact value	Sphere impact value	ROR value
E	GPa	360.0	380.0	380.0	360.0
ν	-	0.22	0.22	0.22	0.22
ρ	kg/m ³	3850	3890	3890	3850
A	GPa	0.930	0.930	0.930	0.930
B	GPa	0.310	0.310	0.310	0.310
n	-	0.6	0.6	0.6	0.6
m	-	0.6	0.6	0.6	0.6
C	-	0.0	0.0	0.0	0.0
T	GPa	0.2	0.2	0.2	0.2
η	GPa·s	$0.028 \cdot 10^{-3}$	$0.028 \cdot 10^{-3}$	$0.028 \cdot 10^{-3}$	$0.028 \cdot 10^{-3}$
λ_t	s ⁻¹	$4 \cdot 10^4$	$4 \cdot 10^4$	$4 \cdot 10^4$	$4 \cdot 10^4$
HEL	GPa	6.25	6.25	6.25	6.25
P_{HEL}	GPa	3.50	3.25	3.25	3.50
σ_{HEL}	GPa	4.125	4.50	4.50	4.125
$\bar{\epsilon}_p^{min}$	-	$1.5 \cdot 10^{-4}$	$1.5 \cdot 10^{-4}$	$1.5 \cdot 10^{-4}$	$1.5 \cdot 10^{-4}$
$\bar{\epsilon}_p^{max}$	-	0.4965	0.4965	0.4965	0.4965
p_t	GPa	-0.17	-0.17	-0.17	-0.17
p_c	GPa	3.02	3.02	3.02	3.02

481 results. This procedure is also visualized in Figure 16, where the top graphs shows the intact material strength with
482 uni-axial loading directions and the bottom graph shows the failure strain. For the failure strain the original and pro-
483 posed formulations are plotted. This procedure shows how simple it is to calibrate the proposed failure strain model,
484 using just two well established experiments.

485 The newly proposed tri-linear failure strain formulation (12) will now be used to simulate spall, plate impact,
486 spherical impact and the ring-on-ring test. If the formulation is an improvement over the original one, all four exper-
487 iments should be matched by the simulations. The JH2-V model parameters used in this final section of the paper,
488 for the various tests, are shown in Table 3. The model parameters related to viscosity and failure are kept the same
489 in all simulations. The only variations in parameters are those in stiffness, density and Hugoniot pressure. These are
490 well justified since the experimentally tested materials showed small variations in the elastic properties, as discussed
491 in section 3.1.

492 Figure 17 provides the predicted spall strength as a function of loading rate, when using the proposed tri-linear
493 failure strain formulation. The rate dependency in the spall strength is still captured by the model. The strengths of
494 the JH2-V model with original and the proposed softening formulation are a very close match. This can be easily
495 explained, as the problem is tension dominated and both formulations used a minimal failure strain $\bar{\epsilon}_p^{min} = 0.00015$
496 (see (10) and (12)). When the failure zone of the simulation is compared to the experiment in Figure 18, it is found
497 that the failure zones agree well.

498 Figure 19 shows the inter-facial velocities measured in the plate impact simulation using the tri-linear failure
499 strain formulation. The results agree well with the experimental results and are quite similar to those obtained with
500 the original JH2 formulation with $d_1 = 0.500$. Again this can be easily explained since the problem is compression
501 dominated and the failure strain in the original or tri-linear formulation is of the same order.

502 Figure 20 shows the damage predicted by a spherical impact simulation using the tri-linear failure strain formula-
503 tion. The results are similar to those for $d_1 = 0.500$ from Figure 12. That is, a cone crack is predicted and some minor
504 subsurface damage is present. Two differences can be found when comparing to the results from Figure 12. The first
505 is that the cone crack for the tri-linear failure strain extends further into the target material. This can be explained by
506 the more brittle behaviour found at tensile states in the new formulation. The second difference is that the tri-linear

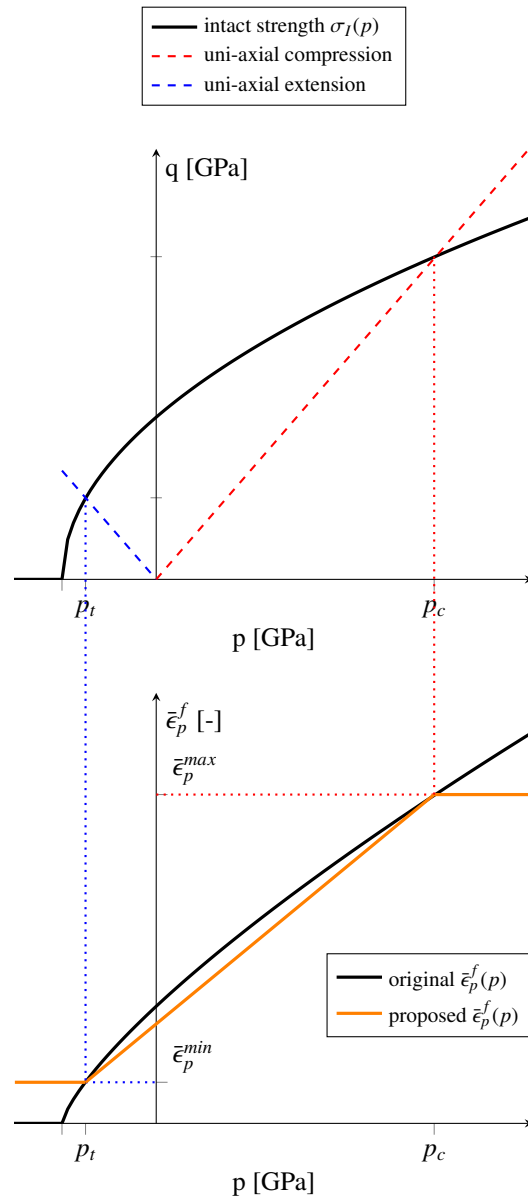


Figure 16: Intact material strength and failure strains plotted as a function of pressure. The original and proposed tri-linear failure strain is shown. The proposed failure strain formulation is fitted to the original failure strains, found under uni-axial deformation of the ceramic.

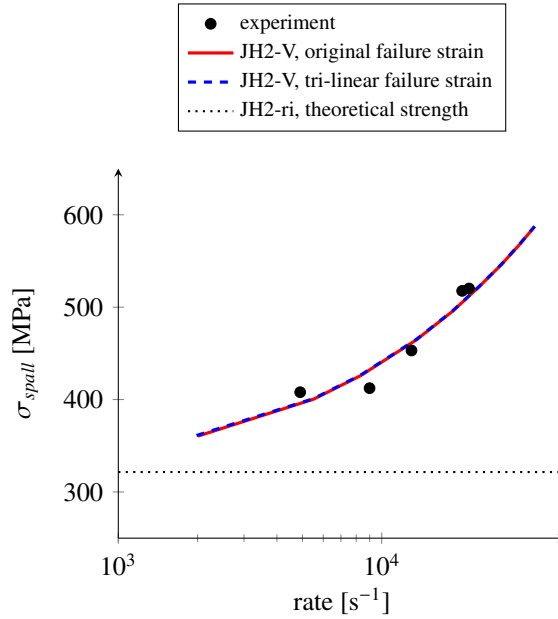


Figure 17: Spall strength, experimentally measured and predicted by simulation. The proposed tri-linear failure strain model is used, all cases use $\eta = 0.028 \cdot 10^{-3} \text{ GPa}\cdot\text{s}$ and $\lambda_t = 40 \cdot 10^3 \text{ s}^{-1}$ as these values were used to obtain good results in spherical impact simulations. A minimal failure strain $\bar{\epsilon}_p^{\text{min}} = 1.5 \cdot 10^{-4}$ is used for both the original and the tri-linear failure strains.

507 formulation results show more damage at the target surface. Again this is a zone where the pressure is low (or even
 508 negative), for which the behaviour is brittle in the tri-linear formulation.

509 As a final step the ring-on-ring simulations are performed with the newly proposed failure strain formulation. A
 510 tensile strength is found of 251MPa. This is slightly higher than the previously found value for the original model
 511 with $d_1 = 0.005$. However, the strength predicted by the newly proposed model still falls within the experimentally
 512 measured ranges (190 – 260MPa from [61] and 168.6 – 232.7MPa from [26]).

513 5. Conclusions

514 A ceramic material may fail as a consequence of different mechanisms. Depending on the stress state in the
 515 material one or more of these failure mechanisms may be activated. Since the mechanisms are different, so should the
 516 modeling of these mechanisms be. The original JH2 model does not distinguish between different failure mechanisms.
 517 In the JH2 model the rate of damage is determined by the failure strain. This failure strain is a function of pressure,
 518 where tensile states have a low strain to failure and a brittle response while high pressures have a high strain to
 519 failure and a more ductile response. The failure strain is, however, a single function and behaviour under tension
 520 and compression are inseparably coupled. By simulating a number of experiments under different loading conditions
 521 it was shown that this single function is indeed incapable of properly capturing the behaviour of the various failure
 522 modes in ceramic material.

523 Four experiments were simulated using the JH2-V model with the original JH2 failure strain formulation. All
 524 experimental results were obtained from literature and in all experiments a similar high purity alumina ceramic was
 525 considered. The first experiment was spall, which loads the material in uni-axial extension. The second experiment
 526 was plate impact, loading the material in uni-axial contraction. Spherical impact was the third experiment, in which
 527 the material experiences a wide range of stress states. As a final test ring-on-ring bending was considered, a quasi-
 528 static test with failure of the material in bi-axial tension.

529 Simulation of spall and plate impact experiments showed that a match for both could only be obtained by changing
 530 the material parameters. Either increasing the residual strength of the material or the failure strain of the material
 531 was required to match the plate impact experiments by simulation. A recalibration of the model parameters would

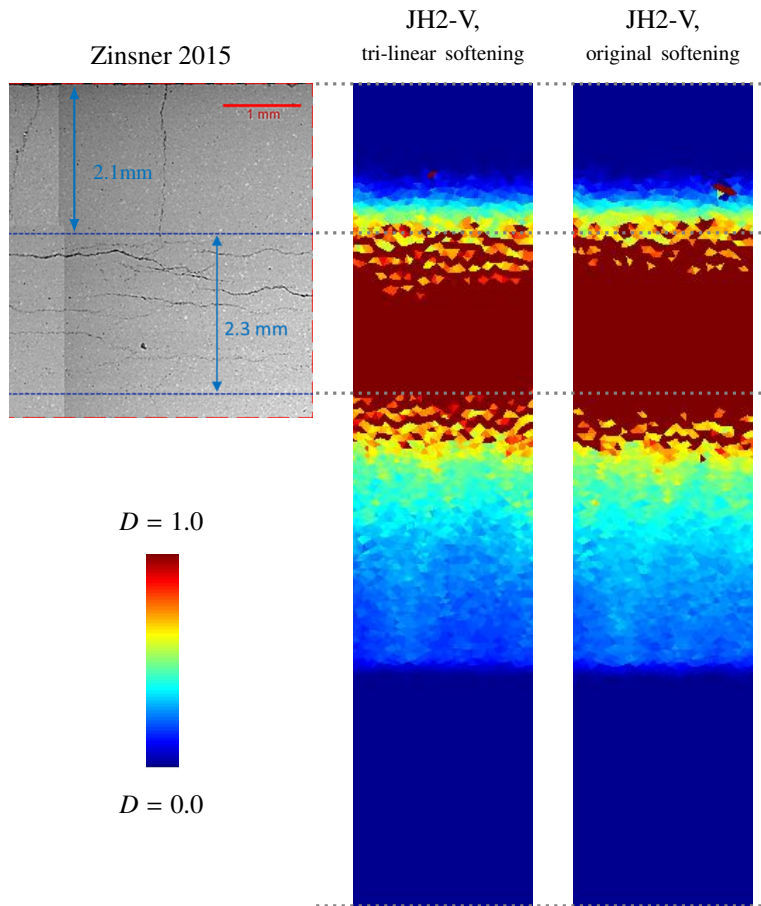


Figure 18: Damage profiles obtained in the spall experiment [26] and FE simulations. Stress wave 2 from Figure 2a is applied. The JH2-V material model with original and newly proposed tri-linear failure strain formulation is compared.

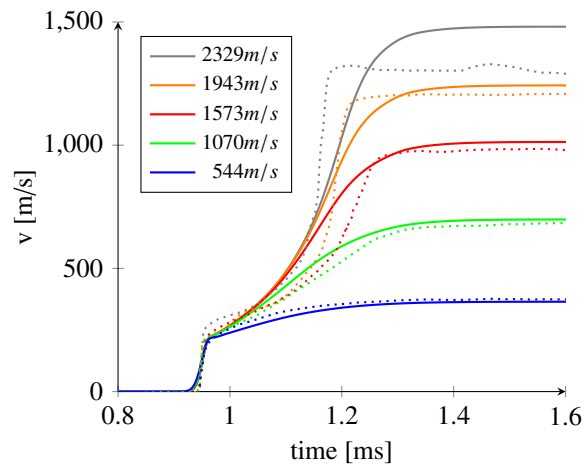


Figure 19: Simulation results for a plate impact test on alumina ceramic. The parameter set for the spall test is used, but with the newly proposed failure strain formulation and $\dot{\lambda}_t = 40000s^{-1}$. The results are very similar to those obtained with the original JH2 formulation with $d_1 = 0.500$ and $\dot{\lambda}_t = 40000s^{-1}$, from Figure 9. The dotted lines show the experimental results from [54], the solid lines are simulation results.

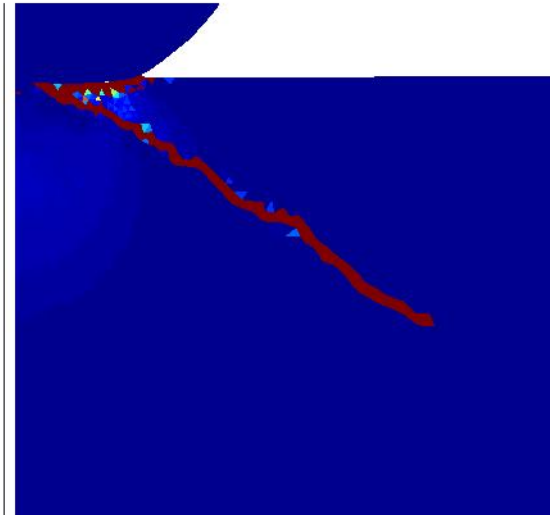


Figure 20: Spherical impact results for the JH2-V model with tri-linear failure strain. Cone cracks are clearly visible, as well as some minor subsurface damage. Complete failure of the ceramic below the projectile is not observed.

532 be sufficient to match both types of tests, although this would increase some model parameters by a few orders of
 533 magnitude compared to what is used in literature.

534 The spherical impact experiments and simulations were used to investigate the parameter choice in the material
 535 model. Increasing the residual strength of the material, which was found to give a match in plate impact results, did
 536 not lead to good results in the spherical impact test. It was found that a match with experiments could only be found
 537 by increasing the failure strain. At this point recalibrating the failure strain parameters would be sufficient to find
 538 matching results of the spall, plate impact and spherical impact tests. However, doing so would require a failure strain
 539 two orders of magnitude larger than what was reported in literature. This could jeopardize the brittle behaviour of the
 540 material under tension.

541 As a final check a ring-on-ring test was simulated. This quasi-static test loads the material in bi-axial tension. It
 542 was shown that the material tensile strength was greatly overestimated when using a high failure strain.

543 The results of the four experiments and simulations showed that the ceramic material required both a high and
 544 a low failure strain, depending on the stress state. The original failure strain formulation in the JH models could
 545 not be tuned to provide this range of failure strains. A new tri-linear formulation was proposed, in which failure
 546 strains under tension and compression were treated as independent quantities. With this formulation a brittle response
 547 could be obtained under tension, while maintaining a ductile response under compression. It was shown that this new
 548 formulation could be used to match all experiments considered in the paper, for a single set of failure parameters. The
 549 latter is key, as this was not possible with the original failure strain formulation.

550 References

- 551 [1] P. J. Hazell, Ceramic Armour: Design and Defeat Mechanisms, Argos Press, Canberra, 2006.
 552 [2] S. M. Walley, Historical review of high strain rate and shock properties of ceramics relevant to their application in armour, Advances in
 553 Applied Ceramics 109 (8) (2010) 446–466. doi:10.1179/174367609X422180.
 554 URL <http://www.maneyonline.com/doi/abs/10.1179/174367609X422180>
 555 [3] Z. Rosenberg, E. Dekel, Terminal ballistics, 2nd Edition, Springer-Verlag, Heidelberg, 2012.
 556 [4] J. Cagnoux, F. Longy, Spallation and shock-wave behaviour of some ceramics, Le Journal de Physique Colloques 49 (C3) (1988) C3–3–C3–
 557 10. doi:10.1051/jphyscol:1988301.
 558 URL <http://www.edpsciences.org/10.1051/jphyscol:1988301>
 559 [5] J. Lankford, C. E. A. Jr, A. J. Nagy, J. D. Walker, A. E. Nicholls, Inelastic response of confined aluminium oxide under dynamic loading
 560 conditions, Journal of Materials Science 33 (1998) 1619–1625.
 561 URL <http://link.springer.com/article/10.1023/A:1017576123026>

- [6] S. Acharya, S. Bysakh, V. Parameswaran, A. Kumar Mukhopadhyay, Deformation and failure of alumina under high strain rate compressive loading, *Ceramics International* 41 (5) (2015) 6793–6801. doi:10.1016/j.ceramint.2015.01.126.
URL <http://dx.doi.org/10.1016/j.ceramint.2015.01.126>
- [7] J. Wade, S. Robertson, H. Wu, Plastic deformation of polycrystalline alumina introduced by scaled-down drop-weight impacts, *Materials Letters* 175 (2016) 143–147. doi:10.1016/j.matlet.2016.04.023.
URL <http://dx.doi.org/10.1016/j.matlet.2016.04.023>
- [8] M. Bhattacharya, S. Dalui, N. Dey, S. Bysakh, J. Ghosh, A. Kumar Mukhopadhyay, Low strain rate compressive failure mechanism of coarse grain alumina, *Ceramics International* 42 (8) (2016) 9875–9886. doi:10.1016/j.ceramint.2016.03.087.
URL <http://linkinghub.elsevier.com/retrieve/pii/S0272884216302231>
- [9] A. C. Fischer-Cripps, B. R. Lawn, Stress Analysis of Contact Deformation in Quasi-Plastic Ceramics, *Journal of the American Ceramic Society* 79 (10) (1996) 2609–2618. doi:10.1111/j.1151-2916.1996.tb09023.x.
- [10] A. A. Wereszczak, T. P. Kirkland, K. T. Strong, T. J. Holmquist, Ornl quasi-static mechanical characterization and analysis : Fy09 annual report to tardec under contract de-ac05-00or22725, Tech. rep., Oak Ridge National Laboratory (2009).
- [11] T. J. Ahrens, Material Strength Effect in the Shock Compression of Alumina, *Journal of Applied Physics* 39 (10) (1968) 4610. doi:10.1063/1.1655810.
URL <http://scitation.aip.org/content/aip/journal/jap/39/10/10.1063/1.1655810>
- [12] W. H. Gust, E. B. Royce, Dynamic Yield Strengths of B4C, BeO, and Al2O3 Ceramics, *Journal of Applied Physics* 42 (1) (1971) 276. doi:10.1063/1.1659584.
- [13] A. M. Rajendran, J. L. Kroupa, Impact damage model for ceramic materials, *Journal of Applied Physics* 66 (8) (1989) 3560–3565. doi:10.1063/1.344085.
- [14] A. M. Rajendran, High Strain Rate Behavior of Metals Ceramics, and Concrete, Tech. rep., University of Dayton Research Institute, Dayton, Ohio (1992).
URL <http://oai.dtic.mil/oai/oai?verb=getRecord&metadataPrefix=html&identifier=ADA252979>
- [15] Y. Partom, Calibrating a material model for AD995 alumina from plate impact VISAR profile, *Journal de Physique IV* 4 (C8) (1994) 495–500.
- [16] D. E. Grady, R. L. Moody, Shock Compression Profiles in Ceramics, Tech. Rep. March, Sandia National Laboratories, Albuquerque (1996).
- [17] D. E. Grady, Shock-wave compression of brittle solids, *Mechanics of Materials* 29 (1998) 181–203. doi:10.1016/S0167-6636(98)00015-5.
- [18] T. J. Vogler, W. D. Reinhart, L. C. Chhabildas, Dynamic behavior of boron carbide, *Journal of Applied Physics* 95 (8) (2004) 4173–4183. doi:10.1063/1.1686902.
- [19] E. B. Zaretsky, High temperature impact response of 998 alumina, *Journal of Applied Physics* 114 (18) (2013) 183518. doi:10.1063/1.4830014.
URL <http://scitation.aip.org/content/aip/journal/jap/114/18/10.1063/1.4830014>
- [20] I. Gurlitsky, E. Zaretsky, S. Kalabukhov, M. P. Dariel, N. Frage, Dynamic compressive and tensile strengths of spark plasma sintered alumina, *Journal of Applied Physics* 115 (24) (2014) 243505. doi:10.1063/1.4885436.
URL <http://scitation.aip.org/content/aip/journal/jap/115/24/10.1063/1.4885436>
- [21] F. Gálvez, J. Rodríguez, V. Sánchez, Tensile strength measurements of ceramic materials at high rates of strain, *Journal of physics IV France* 7 (1997) 151–155.
URL <http://jp4.journaldephysique.org/articles/jp4/abs/1997/03/jp4199707C328/jp4199707C328.html>
- [22] F. Gálvez, J. Rodríguez, V. Sánchez Galvez, Influence of the Strain Rate on the Tensile Strength in Aluminas of Different Purity, *Journal of Physics IV* 10 (2000) 323–328.
- [23] F. G. Díaz-Rubio, J. R. Pérez, V. S. Gálvez, The spalling of long bars as a reliable method of measuring the dynamic tensile strength of ceramics, *International Journal of Impact Engineering* 27 (2002) 161–177.
URL <http://www.sciencedirect.com/science/article/pii/S0734743X01000392>
- [24] J. Buchar, S. Rolc, Dynamic fracture of ceramics, *Journal de Physique IV (Proceedings)* 134 (2006) 681–686. doi:10.1051/jp4:2006134105.
- [25] B. Erzar, E. Buzaud, Shockless spalling damage of alumina ceramic, *European Physical Journal: Special Topics* 206 (1) (2012) 71–77. doi:10.1140/epjst/e2012-01588-0.
- [26] J.-L. Zinszner, B. Erzar, P. Forquin, E. Buzaud, Dynamic fragmentation of an alumina ceramic subjected to shockless spalling: An experimental and numerical study, *Journal of the Mechanics and Physics of Solids* 85 (2015) 112–127. doi:10.1016/j.jmps.2015.08.014.
URL <http://dx.doi.org/10.1016/j.jmps.2015.08.014>
- [27] J.-L. Zinszner, B. Erzar, P. Forquin, Strain rate sensitivity of the tensile strength of two silicon carbides: experimental evidence and micromechanical modelling, *Philosophical Transactions of the Royal Society of London A: Mathematical, Physical and Engineering Sciences* 375 (2085). arXiv:<http://rsta.royalsocietypublishing.org/content/375/2085/20160167.full.pdf>, doi:10.1098/rsta.2016.0167.
URL <http://rsta.royalsocietypublishing.org/content/375/2085/20160167>
- [28] G. R. Johnson, T. J. Holmquist, A computational constitutive model for brittle materials subjected to large strains, high strain rates, and high pressures, *Shock Wave and High-Strain-Rate Phenomena in Materials*.
- [29] G. R. Johnson, T. J. Holmquist, An improved computational constitutive model for brittle materials, *AIP Conference Proceedings* 309 (1994) 981–984. doi:10.1063/1.46199.
URL <http://scitation.aip.org/content/aip/proceeding/aipcp/10.1063/1.46199>
- [30] G. R. Johnson, T. J. Holmquist, S. R. Beissel, Response of aluminum nitride (including a phase change) to large strains, high strain rates, and high pressures, *Journal of Applied Physics* 94 (3) (2003) 1639. doi:10.1063/1.1589177.
URL <http://scitation.aip.org/content/aip/journal/jap/94/3/10.1063/1.1589177>
- [31] C. Simha, S. J. Bless, A. Bedford, Computational modeling of the penetration response of a high-purity ceramic, *International journal of impact engineering* 27 (2002) 65–86.

- 627 URL <http://www.sciencedirect.com/science/article/pii/S0734743X01000367>
- 628 [32] V. S. Deshpande, A. G. Evans, Inelastic deformation and energy dissipation in ceramics: A mechanism-based constitutive model, *Journal of*
629 *the Mechanics and Physics of Solids* 56 (10) (2008) 3077–3100. doi:10.1016/j.jmps.2008.05.002.
630 URL <http://linkinghub.elsevier.com/retrieve/pii/S0022509608000975>
- 631 [33] V. S. Deshpande, E. A. N. Gamble, B. G. Compton, R. M. McMeeking, A. G. Evans, F. W. Zok, A Constitutive Description of the Inelastic
632 Response of Ceramics, *Journal of the American Ceramic Society* 94 (2011) s204–s214. doi:10.1111/j.1551-2916.2011.04516.x.
633 URL <http://doi.wiley.com/10.1111/j.1551-2916.2011.04516.x>
- 634 [34] E. C. Simons, J. Weerheijm, L. J. Sluys, A viscosity regularized plasticity model for ceramics, *European Journal of Mechanics / A Solids*
635 72 (July 2017) (2018) 310–328. doi:10.1016/j.euomechsol.2018.05.009.
636 URL <https://doi.org/10.1016/j.euomechsol.2018.05.009>
- 637 [35] A. Needleman, Material rate dependence and mesh sensitivity in localization problems, *Computer Methods in Applied Mechanics and Engi-*
638 *neering* 67 (1) (1988) 69–85. doi:10.1016/0045-7825(88)90069-2.
- 639 [36] W. Wang, L. Sluys, R. De Borst, Interaction between material length scale and imperfection size for localisation phenomena in viscoplastic
640 media, *European Journal of Mechanics - A/Solids* 15 (3) (1996) 447–464.
- 641 [37] A. Winnicki, C. J. Pearce, N. Bićanić, Viscoplastic Hoffman consistency model for concrete, *Computers and Structures* 79 (1) (2001) 7–19.
642 doi:10.1016/S0045-7949(00)00110-3.
- 643 [38] Dynaflo Research Group, Jem-jive.
644 URL <http://jem-jive.com>
- 645 [39] D. Sulsky, Z. Chen, H. L. Schreyer, A particle method for history-dependent materials, *Computer Methods in Applied Mechanics and*
646 *Engineering* 118 (1-2) (1994) 179–196. doi:10.1016/0045-7825(94)90112-0.
- 647 [40] F. Li, J. Pan, C. Sinka, Modelling brittle impact failure of disc particles using material point method, *International Journal of Impact Engi-*
648 *neering* 38 (7) (2011) 653–660. doi:10.1016/j.ijimpeng.2011.02.004.
649 URL <http://dx.doi.org/10.1016/j.ijimpeng.2011.02.004>
- 650 [41] L. B. Lucy, A numerical approach to the testing of the fission hypothesis, *The Astronomical Journal* 82 (12) (1977) 1013–1024.
- 651 [42] J. J. Monaghan, Smoothed particle hydrodynamics, *Annual Review of Astronomy and Astrophysics* 30 (september) (1992) 543–574. doi:
652 10.1088/0034-4885/68/8/R01.
653 URL [http://iopscience.iop.org/0034-4885/68/8/R01\\$delimitter"026E30F\\$nhhttp://arxiv.org/abs/1007.1245](http://iopscience.iop.org/0034-4885/68/8/R01$delimitter)
- 654 [43] R. Clegg, Development and application of a Rankine plasticity model for improved prediction of tensile cracking in ceramic and concrete
655 materials under impact, 14th DYMAT Technical Meeting.
656 URL <http://hsrlab.gatech.edu/AUTODYN/papers/paper143.pdf>
- 657 [44] E. Strassburger, Visualization of Impact Damage in Ceramics Using the Edge-On Impact Technique, *International Journal of Applied Ceramic*
658 *Technology* 1 (3) (2005) 235–242. doi:10.1111/j.1744-7402.2004.tb00175.x.
659 URL <http://doi.wiley.com/10.1111/j.1744-7402.2004.tb00175.x>
- 660 [45] W. Riedel, S. Hiermaier, K. Thoma, Transient stress and failure analysis of impact experiments with ceramics, *Materials Science and Engi-*
661 *neering B: Solid-State Materials for Advanced Technology* 173 (1-3) (2010) 139–147. doi:10.1016/j.mseb.2009.10.038.
662 URL <http://dx.doi.org/10.1016/j.mseb.2009.10.038>
- 663 [46] H. Zolghadr Jahromi, B. A. Izzuddin, Energy conserving algorithms for dynamic contact analysis using newmark methods, *Computers and*
664 *Structures* 118 (2013) 74–89. doi:10.1016/j.compstruc.2012.07.012.
- 665 [47] J. Ning, H. Ren, T. Guo, P. Li, Dynamic response of alumina ceramics impacted by long tungsten projectile, *International Journal of Impact*
666 *Engineering* 62 (2013) 60–74. doi:10.1016/j.ijimpeng.2013.06.006.
667 URL <http://dx.doi.org/10.1016/j.ijimpeng.2013.06.006>
- 668 [48] H. L. Ren, X. F. Shu, L. I. Ping, Numerical and experimental investigation of the fracture behavior of shock loaded alumina, *Science China:*
669 *Physics, Mechanics and Astronomy* 53 (2) (2010) 244–252. doi:10.1007/s11433-009-0267-y.
- 670 [49] S. Feli, M. R. Asgari, Finite element simulation of ceramic/composite armor under ballistic impact, *Composites Part B: Engineering* 42 (4)
671 (2011) 771–780. doi:10.1016/j.compositesb.2011.01.024.
672 URL <http://linkinghub.elsevier.com/retrieve/pii/S1359836811000527>
- 673 [50] P. Lundberg, Interface Defeat and Penetration : Two Modes of Interaction between Metallic Projectiles and Ceramic Targets, *Comprehensive*
674 *Summaries of Uppsala Dissertations from the Faculty of Science and Technology*.
- 675 [51] R. Krashanitsa, S. Shkarayev, Computational Study of Dynamic Response and Flow Behavior of Damaged Ceramics, in: 46th
676 AIAA/ASME/ASCE/AHS/ASC Structures, Structural Dynamics and Materials Conference, 2005, pp. 1–8. doi:10.2514/6.2005-1847.
677 URL <http://arc.aiaa.org/doi/10.2514/6.2005-1847>
- 678 [52] C. Swaroop, A. K. Srivastava, Numerical Analysis of Ballistic Performance of Curved Ceramic, in: *Proceeding of STME-2013, International*
679 *Conference on Smart Technologies for Mechanical Engineering*, Delhi, 2013.
- 680 [53] A. Tasdemirci, I. W. Hall, Numerical and experimental studies of damage generation in multi-layer composite materials at high strain rates,
681 *International Journal of Impact Engineering* 34 (2) (2007) 189–204. doi:10.1016/j.ijimpeng.2005.08.010.
- 682 [54] D. E. Grady, *Dynamic Properties of Ceramic Materials*, Tech. Rep. February, Sandia National Laboratories, Albuquerque (1995).
- 683 [55] T. J. R. Hughes, Generalization of Selective Integration Procedures to Anisotropic and Nonlinear Media, *Short Communications* 15 (9) (1980)
684 1413–1418. doi:10.1002/nme.1620150914.
- 685 [56] B. G. Compton, E. A. N. Gamble, V. S. Deshpande, F. W. Zok, Damage development in an armor alumina impacted with ductile metal
686 spheres, *Journal of Mechanics of Materials and Structures* 7 (6).
- 687 [57] K. A. Iyer, Relationships between multiaxial stress states and internal fracture patterns in sphere-impacted silicon carbide, *International*
688 *Journal of Fracture* 146 (1-2) (2007) 1–18. doi:10.1007/s10704-007-9108-z.
- 689 [58] E. K. Öberg, J. Dean, T. W. Clyne, Effect of inter-layer toughness in ballistic protection systems on absorption of projectile energy, *Internat-*
690 *ional Journal of Impact Engineering* 76 (2015) 75–82. doi:10.1016/j.ijimpeng.2014.09.006.
- 691 [59] A. F. Kirstein, R. M. Woolley, Symmetrical bending of thin circular elastic plates on equally spaced point supports, *Journal of Research of*

- 692 the National Bureau of Standards, Section C: Engineering and Instrumentation 71C (1) (1967) 1–10. doi:10.6028/jres.071C.002.
- 693 [60] C. H. Hsueh, C. R. Luttrell, P. F. Becher, Modelling of bonded multilayered disks subjected to biaxial flexure tests, *International Journal of*
694 *Solids and Structures* 43 (20) (2006) 6014–6025. doi:10.1016/j.ijsolstr.2005.07.020.
- 695 [61] B. J. de Smet, P. W. Bach, H. F. Scholten, L. J. M. G. Dortmans, G. de With, Weakest-link failure predictions for ceramics III: Uniaxial and
696 biaxial bend tests on alumina, *Journal of the European Ceramic Society* 10 (2) (1992) 101–107. doi:10.1016/0955-2219(92)90124-V.
- 697 [62] T. J. Holmquist, G. R. Johnson, C. a. Gerlach, An improved computational constitutive model for glass, *Philosophical Transactions of the*
698 *Royal Society A: Mathematical, Physical and Engineering Sciences* 375 (2085). doi:10.1098/rsta.2016.0182.
- 699 [63] H. C. Heard, C. F. Cline, Mechanical behaviour of polycrystalline BeO, Al₂O₃ and AlN at high pressure, *Journal of Materials Science* 15 (8)
700 (1980) 1889–1897. doi:10.1007/BF00550614.
- 701 [64] E. B. Zaretsky, V. E. Paris, G. I. Kanel, A. S. Savinykh, Evidences of ductile and brittle responses of ceramics under shock wave loading,
702 *Journal de Physique IV* 2 110 (2003) 917–922.
- 703 [65] E. B. Zaretsky, V. E. Paris, G. I. Kanel, A. S. Savinykh, Evidence of Ductile (Alumina) and Brittle (Boron Carbide) Response of Ceramics Un-
704 der Shock Wave Loading, *Ceramic Transactions* 151 (2003) 105–115. arXiv:arXiv:1011.1669v3, doi:10.1017/CB09781107415324.
705 004.